# Inelastic collisions of atomic thorium and molecular thorium monoxide with cold helium-3

# Inelastic Collisions of Atomic Thorium and Molecular Thorium Monoxide with Cold Helium-3

A dissertation presented

by

Yat Shan Au

to

The Department of Physics

in partial fulfillment of the requirements

for the degree of

Doctor of Philosophy

in the subject of

Physics

Harvard University

Cambridge, Massachusetts

November 2013

Dissertation advisor

**Professor John Morrissey Doyle**

Author

**Yat Shan Au**

# Inelastic Collisions of Atomic Thorium and Molecular Thorium Monoxide with Cold Helium-3

## Abstract

We measure inelastic cross sections for atomic thorium (Th) and molecular thorium monoxide (ThO) in collisions with $^3$He at temperatures near 1 K. We determine the Zeeman relaxation cross section for Th ($^3F_2$) to be $\sim 2 \times 10^{-17}$ cm$^{-2}$ at 800 mK. We study electronic inelastic processes in Th ($^3P_0$) and find no quenching even after $10^6$ collisions at 800 mK. We measure the vibrational quenching cross section for ThO (X, $\nu = 1$) to be $(7.9 \pm 2.7) \times 10^{-19}$ cm$^{-2}$ at 800 mK. Finally, we observe indirect evidence for ThO (X, $\nu = 0$)–$^3$He van der Waals complex formation, and measure the 3-body recombination rate constant to be $\Gamma_3 = (8 \pm 2) \times 10^{-33}$ cm$^6$s$^{-1}$ at 2.4 K. The stability of the ground Th ($^3F_2$) state, metastable Th ($^3P_0$) state, and vibrational excited ThO (X, $\nu = 1$) state provides data on anisotropic interactions in new systems and opens up the possibility for further studies and experiments, including trapping.

# Contents

# List of Figures

# List of Tables

# Citations to Previously Published Work

Portions of this thesis have appeared previously in the following papers:

> "Vibrational quenching of the electronic ground state in ThO in cold collisions with $^3$He," Yat Shan Au, Colin B. Connolly, Wolfgang Ketterle, and John M. Doyle, arXiv:1310.7279 [physics.atom-ph] (2013) [1].
>
> "Properties of the ground $^3F_2$ state and the excited $^3P_0$ state of atomic thorium in cold collisions with $^3$He," Yat Shan Au, Colin B. Connolly, Wolfgang Ketterle, and John M. Doyle, arXiv:1310.7264 [physics.atom-ph] (2013) [2].

# Acknowledgements

I thank my advisor, John Doyle, for pragmatic guidance on every project and Wolfgang Ketterle, for insightful scientific and technical advice. I also acknowledge my colleagues, family, and friends for their unrelenting help and support.

# Chapter 1

# Introduction

Since the first demonstration of laser cooling of atoms in the 1970s and 80s [3, 4], the science of cold atoms has expanded far beyond just the control of their classical motion, to quantum control of internal and external states. Compared to fabricated devices, the structures of every individual atom and molecule are determined by inherent quantum mechanisms and therefore leads to perfectly identical particles. This "standardization" has led to applications and improvements in atomic clocks [5], gravity gradient sensing [6, 7] and precision measurement of fundamental constants [8–12]. Manipulations of the internal quantum states of atoms has led to the demonstration of quantum computing and quantum communication [13, 14]. The creation of Bose-Einstein Condensation [15, 16] and degenerate Fermi gases [17, 18], and the subsequent tuning of interactions between atoms with external fields has been exploited to study physics previously occurring only in condensed matter systems [19, 20].

In the last decade, the field has advanced dramatically. The invention of the optical frequency comb [21] could replace the microwave frequency standard with an optical standard [22]. The control and manipulation of cold molecules have led to an order of magnitude improvement in the electron EDM limit [23, 24]. Hybrid quan-

tum devices connecting ultracold atoms to solid-state systems, which could possess properties absent in the constituent systems, have recently been realized [25, 26]. Quantum simulation have begun the exploration of synthetic Hamiltonians [27–29].

Over the same period, the availability of cold atoms and molecules has expanded to over half of the elements in the periodic table and has included now half a dozen molecules. This diversification of cold atomic and molecular species, and the advancement of cold atom technologies is not merely coincidental. Only a few applications do not utilize the specific structure of an element [6, 7], and many experiments can benefit from certain specific properties of an atomic species. For example, since dipolar interactions scale with the square of the magnetic moment, this interaction has only been observed (away from zero-crossings of scattering length) in elements with a magnetic moment larger 6 $\mu_B$ [30–32], of which there are few. In a proposed scheme to couple a rotational state of a polar molecule and a Josephson junction via a microwave photon [33], there are tremendous technological differences between a molecule with a rotational constant in the 3 GHz range and one in the 30 GHz range (the latter being nearly impossible). Precision measurement applications rely entirely on specific atomic and molecular structures, especially relativistic effects in very heavy atoms [34]. The natural linewidth of an atomic transition will set the ultimate limit on the precision of an atomic clock [35] and specific energy level structures place practical limits on systemic errors in those systems [36]. The new limit on the electron EDM depends on the enhancement factor (magnitude of the molecular internal field) in ThO and systematic error suppression as provided by the particular features of $\Omega$-doubling [24].

## 1.1 Sources of cold atoms and molecules

Using laser cooling, evaporative cooling [37], Feshbach resonances [38] and photo association [39] diatomic molecules can be assembled from ultracold atoms. These molecules can then be transferred to their absolute ground state without substantial heating [40]. This technique had led to the demonstration of quantum state dependent chemical reactions [41] and dipolar interactions [42]. Despite the enormous success of laser cooling, the requirement to scatter a large number ($\gtrsim 10^4$) of photons during the cooling process [43] has limited its application to alkali-like atoms and a few diatomic molecules [44–46]. In the quest to further diversify the portfolio of cold atoms and molecules, a range of techniques have been developed: kinematic cooling [47, 48], deceleration of a supersonic beam [49, 50], and buffer gas cooling [51].

In Stark deceleration, molecules are cooled using a supersonic expansion to a temperature of a few K in the center-of-mass frame (with a forward velocity of hundreds of m $s^{-1}$ in the lab frame), which are then slowed by forcing them to climb a series of potential hills created by the D.C. Stark shift. When the molecules reach the top of the hills, the acceleration of the downhill motion is prevented by rapidly turning off the electric field. Stark deceleration had led the trapping of CO [52] and $ND_3$ [53]. Trapped OH produced using this method has led to demonstration of evaporative cooling via elastic molecule-molecule collisions [54].

Buffer gas cooling is a widely applicable technique that cools atoms and molecules. Cooling to $\sim 0.5$ K is performed via elastic collisions with an inert, cryogenic buffer gas, such as helium. The cooling process is independent of the internal structures of the colliding partners. Since the invention of the method in 1995, over 25 atoms and 6 molecules [55, 56] have been cooled below 5 K. Buffer gas cooling has led to

the creation of a Bose condensate without the use of laser cooling [57] (second of its kind besides the hydrogen BEC [58] which uses unique surface properties), and magnetic trapping of NH [59] and CaF [43]. Cryogenic buffer gas beams (CBGBs) have led to an improved sensitivity to the electron EDM [24, 60], differentiation of chiral molecules [61], and direct laser cooling of diatomic molecules [45, 46].

## 1.2 Cold collisions and anisotropy

The presence of atomic collisions during the cooling phase makes buffer gas cooling a useful platform for studying cold collisions. Due to the relatively simple, essentially structureless, electronic structure of helium, atom-helium collisions often provide useful links between theory and experiments. Cold collisions are distinct from collisions at higher temperatures in their sensitivity to the interaction potentials. At high temperatures, inelastic collisions can be described by the Langevin capture model. In this model, an inelastic collision occurs with unity probability if there is sufficient total energy to overcome the barrier of the effective interaction potential. Otherwise, the collision is completely elastic. This model is sufficiently accurate for collisions at temperatures $\gtrsim$ 10 K. At lower temperatures, Feshbach and shape resonances [38, 62], which depend on the details of the interaction potentials, can modify the inelastic cross sections by several orders of magnitude. Therefore, cold collisions provide a rare opportunity for probing atomic interaction potentials along with internal structure of the atom or molecule.

Cold inelastic collisions can often be understood in term of interaction anisotropy. At a finite distance, the internal structures of an atom or a molecule breaks spatial symmetry, and this information is revealed to the outside world through interactions (i.e. collisions). Spatial symmetry is broken by the orientation of the electronic

spin and orbital angular momentum, the rotational axis and nuclear motion along the internuclear axis in Zeeman relaxation of an atom or a molecule, and rotational and vibrational quenching of a molecule. Although the actual inelastic rate depends on details of the interaction potentials and the processes involved, large interaction anisotropy generally leads to higher inelastic rates [62]. Although electronic quenching of metastable states is not generally understood, electronic de-excitations typically involve mixing of neighboring states with difference electronic orbital angular momentum, and therefore, interaction anisotropy probably plays a role in these processes.

Interaction anisotropy can be modified in a number of ways. In Zeeman relaxation of most non-S state transition metals [63] and the lanthanides [64], the electrostatic anisotropy of the valence d- and f-orbitals is "shielded" by the presence of outer s-electrons, which limits the atom-atom separation during a cold collision with helium. In Zeeman relaxation of the Ag-He system, anisotropy in the hyperfine interaction is enhanced by the formation of van der Waals molecules [65].

Understanding the physics of inelastic collisions is not only interesting, but also it is important for practical experimental implementations. Zeeman relaxation rates determine the feasibility of magnetic trapping, sympathetic cooling and evaporative cooling of atoms and molecules. Vibrational quenching rates determine whether buffer gas cooling can produce high phase-space density of molecules. van der Waals cluster formation will ultimately limit the applications of buffer gas cooling to large molecules [56]. Understanding inelastic processes is therefore becoming more important as the field is shifting towards larger molecules.

## 1.3 This thesis

In this thesis, we will provide new experiments that examine cold collisions of atomic thorium and molecular thorium monoxide with $^3$He. By measuring the Zeeman relaxation rate of Th ($^3F_2$), we provide quantitative study of anisotropy reduction by "submerged-shell" physics among the actinides. This work will complete the study of Zeeman relaxation across the periodic table. By determining the vibrational quenching rate of ThO (X, $\nu = 1$), we provide a rare experimental data point for vibrational cooling efficiency. We observe indirect evidence for ThO ($\nu = 0$)–$^3$He van der Waals complex formation, among with measurement of the 3-body recombination rate constant. Finally, we study the poorly understood metastable collisions of Th ($^3P_0$) and ThO (H, $\nu = 0$), providing new data that adds to the increasing puzzle of electronic metastable state quenching.

## 1.4 Previous work

When I joined the lab in 2008, it was an exciting time for the science of buffer gas cooling. "Submerged-shell" physics had led to the trapping of 7 rare-earth atoms [64], metastable helium was Bose-condensed without the use of laser cooling [57], and the magnetic trapping and thermal isolation of NH has just been accomplished [59].

In my first two years, I worked with Nathan Brahms, Bonna Newman and Colin Connolly to examine collisions among trapped rare-earth atoms. We discovered that "submerged-shell" physics does not apply to collisions between two non-S state atoms [66, 67]. We also looked for and found the extremely slow spin-exchange between the electron spin in potassium and the nuclear spin in $^3$He [68]. Around the same time, we started to question the central assumption of buffer gas cooling: the inert nature

of helium in the cooling process. After seeing strong indirect evidence for the Ag-$^3$He molecule, Nathan and I spent two months searching for Ag-$^3$He van der Waals molecules [69]. Although our effort did not lead to any direct evidence, our work had generated interests in the Weinstein Lab in Nevada, and they later reported spectroscopic detection of Li-$^4$He molecules [70].

In the next two years, Colin and I started an effort to produce cold NH molecules in our dilution-refrigerator-cooled cell. We experimented with a number of production mechanisms, including "puffing" nitrogen and hydrogen gases into our subkelvin cell, and we built an improved detection system with a collection lens at 4 K, but we were not able to detect trapped NH molecules [71].

After our endeavor with molecules, we refocused our effort on atoms. Shortly after our return to the periodic table, our worst technical nightmare was realized. Our fridge developed a pressure dependent low temperature leak. Fortunately, Colin and I were able to "side-step" the leak and finished our exploration with antimony [72], aluminum [73], thorium [2] and even a molecule, thorium monoxide [1], the results of the last two being the contents of this thesis. Partly because of the sky-rocketing cost of liquid helium, the group emptied the room at the end of the experiment run, and it is now home to two new experiments, one on laser cooling of molecules, the other on microwave detection of very large molecules.

## 1.5 Thesis outline

This thesis describes measurements of inelastic collisions in cold collisions of atomic thorium and molecular thorium monoxide with $^3$He. These measurements probe translational-to-electronic and translation-to-vibrational energy transfer in cold collisions. We extend previous studies [63, 64] on anisotropy reduction in "submerged-

shell" atoms to include the actinides, and thus completing the overview of Zeeman relaxation across the periodic table. We study van der Waals molecules formation in ThO-He collisions. Because of the high binding energy between large molecule and helium, it is reasonable to expect cluster formation, if an allowed pathway is present. Cluster formation via the Lindemann mechanism [74] was explored in Ref. [56]. In the thesis, we focus on the 3-body recombination process. We also study vibration quenching of the ThO (X, $\nu = 1$). As the number of vibrational modes increases rapidly with the size of a molecule, the efficiency of vibrational cooling becomes more important for concentrating population in a few quantum states. This could be critical for obtaining sufficient signal-to-noise in applications such as chemical mixture [75] and chiral analysis [61, 76]. Finally, we study the poorly understood metastable collisions of Th ($^3P_0$) and ThO (H, $\nu = 0$), processes in which interaction anisotropy probably plays a role.

Chapter 2 describes the technique of buffer gas cooling, the experimental method used in this work.

Chapter 3 describes the measurements with atomic thorium. We measure Zeeman relaxation rate of the ground state, search for electronic quenching and set a bound on the radiative lifetime of the metastable first excited state.

Chapter 4 describes the work with molecular thorium monoxide. We observe indirect evidence for ThO-He van der Waals complex formation, measure the vibrational quenching rate of the electronic ground state, search for electronic quenching and set bounds on the radiative lifetime of the metastable H state.

Based on our results, Chapter 5 outlines the practical limits and the future directions for buffer gas cooling of atoms and molecules.

# Chapter 2

# Buffer gas cooling

This chapter describes the experimental techniques used to produce samples of cold atoms and molecules and to measure inelastic collisions.

## 2.1 Parameters for buffer gas cooling

Cooling of a physical object is generally achieved by bringing it into thermal contact with a lower temperature reservoir. In the case of laser cooling, atoms thermalize with an optical field at "zero" temperature. Apart from the only exception of (one isotope of) hydrogen and superfluid $^4$He [77], atoms will stick to any cold surface below 1 K with close to unity probability. In order to cool atoms with a cryogenic cell, an inert buffer gas can be used as a heat link between the atoms and the cold cell wall. A high density buffer gas can additionally be employed to increase lifetime of the atoms in a cell by enforcing diffusive motion.

In a typical buffer gas cooling experiment, an atomic or molecular species is introduced into the buffer gas cell via laser ablation of a solid state precursor (or capillary filling) [78]. Atoms (with mass $M_A$) in the resulting ablation plume at

$T(N = 0) \sim 10^3$ K thermalize with the buffer gas (with mass $m_b$) at $T_b \sim 1$ K via elastic collisions. The energy removed in a single collision is determined by both temperature and mass mismatch [51],

$$k_B \Delta T = k_B (T - T_b) \frac{2 M_A m_b}{(M_A + m_b)^2} = k_B \frac{(T - T_b)}{\kappa}. \tag{2.1}$$

After $N$ collisions, the temperature $T(N)$ of the atoms becomes

$$T(N) = T_b + (T(0) - T_b) e^{(-N/\kappa)}. \tag{2.2}$$

For $M_A/m_b \sim 50$, it takes on the order of 100 collisions to thermalize the atoms to about 1 K. In order to cool the atoms before they reach the cell wall, the mean free path of the atoms must be much smaller than the dimension of the cell. Given a typical elastic cross section $\sigma_{el} \approx 10^{14}$ cm$^{-3}$ and a cell diameter $d \sim 10$ cm, a buffer gas density of $\sim 10^{16}$ cm$^{-3}$ is required. In principle, even higher buffer gas density can be used, but the reduced mean free path may preclude the atoms from populating the bulk of the cell.

As shown in Fig. 2.1, only helium has sufficient equilibrium vapor density for producing cold atom samples below 4 K. At temperatures above 15 K, neon (and hydrogen, at least in principle), can be used to produce cryogenic buffer gas beam sources (CBGBs) [80].

Once the atoms have thermalized with the buffer gas, their motions become diffusive and the atom density $n(\vec{r}, t)$ is given by [81]:

$$\frac{\partial n}{\partial t} = D \nabla^2 n(\vec{r}), \tag{2.3}$$

$$D = \frac{3\pi}{32} \frac{\bar{\nu}}{n_b \sigma_d}, \tag{2.4}$$

$$\bar{\nu} = \sqrt{\frac{8 k_B T}{\pi \mu}}, \tag{2.5}$$

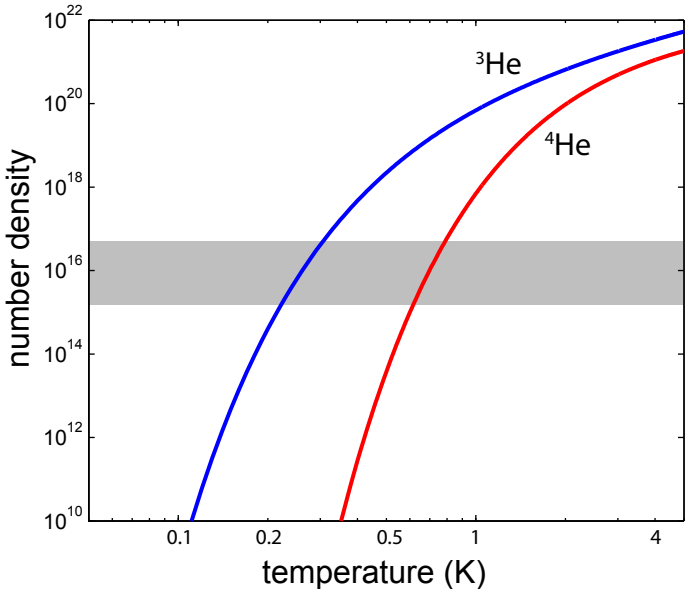


Figure 2.1: Saturated vapor density curves below 5 K [79]. Buffer gas cooling of atoms and molecules typical operates within the shaded band.

where $D$ is the diffusion constant, $n_b$ is the buffer gas density, $\sigma_d$ is the momentum transfer cross section, $\mu$ is the reduced mass of the atom-He system, and $\bar{\nu}$ is the mean center of mass speed.

For a cylindrical cell of radius $R$ and length $L$, the time-dependent atom density $n(\vec{r},t)$ is[1] [82]:

$$n(\vec{r},t) = n(\vec{r}=0)J_0\left(\frac{j_{01}r}{R}\right)\cos\left(\frac{\pi z}{L}\right)e^{-t/\tau_d}, \tag{2.6}$$

$$\tau_d = \frac{32}{3\pi}\frac{n_b\sigma_d}{\bar{v}}\left(\frac{j_{01}^2}{r^2}+\frac{\pi^2}{L^2}\right)^{-1} \tag{2.7}$$

where $j_{01} \approx 2.405$ is the first zero of the Bessel function $J_0(r)$.

[1]We are neglecting the more rapidly decaying higher-order diffusion modes.

### 2.1.1 Momentum-transfer cross section and elastic rate

In the above discussion on the diffusive motion of the atoms, we have been using the momentum-transfer cross section $\sigma_d$, as opposed to the elastic cross section $\sigma_{el}$ as reported in many theory calculations.

In the ideal case, the experimenter has control over all collisional parameters. The collision rate constant $k_{el}$ is given by

$$k_{el}(\theta, E) = \sigma_{el}(\theta, E)\nu(E) \tag{2.8}$$

where $\nu = \sqrt{2E/m}$ is the center-of-mass collisional speed.

A crossed atomic beam experiment with angular resolution is an example. State-of-the-art Stark decelerated beams can probe energies above 30 K [83]. In order to access lower collision energies ($\sim 0.5$ K), one might be willing to trade-in both angular and energy resolution. Averaging over both collisional angle and thermal energy, $k_{el}$ becomes

$$k_{el} = \iint dE d\theta [\sigma_{el}(\theta, E)\nu(E) f_{MB}(E)] = \int dE [\sigma_{el}\nu(E) f_{MB}(E)] \tag{2.9}$$

where $f_{MB}$ is the Maxwell-Boltzmann distribution.

Since the measurements presented in this thesis rely on the diffusion time of the atoms to calibrate the helium density and hence the collision rate, our results are sensitive to the momentum-transfer cross section $\sigma_d$ instead of $\sigma_{el}$:

$$\sigma_d = \int d\theta [(1 - \cos(\theta))\sigma_{el}(\theta) \sin(\theta)] \tag{2.10}$$

The effect of the $(1 - \cos(\theta))$ weighting function is to weaken the contribution from small scattering angles.

Table 2.1: Absolute diffusion cross sections. † denotes primary calibration.

| System | Temperature (K) | $\sigma_d$ ($10^{-14}$ cm$^2$) |
|---|---|---|
| $^4$He*-$^4$He | 0.4 | $0.26(^{+0.3}_{-0.1})$ [84] |
| Sc-$^3$He | 0.8 | $1.3 \pm 0.6$ [85] |
| Ti-$^3$He | 0.8 | $1.5 \pm 0.6$ [85] |
| Cr-$^3$He† | 0.3 | $1.1 \pm 0.4$ [86] |
| Mn-$^3$He | 0.6 | 1.0 [84] |
| Y-$^3$He | 0.8 | $1.4 \pm 0.6$ [85] |
| Sb-$^4$He | 0.8 | $0.57 \pm 0.07$ [71] |
| Pr-$^3$He | 0.8 | $1.3 \pm 0.6$ [85] |
| Nd-$^3$He | 0.8 | $1.3 \pm 0.6$ [85] |
| Tb-$^3$He | 0.8 | $1.9 \pm 0.6$ [85] |
| Dy-$^3$He | 0.8 | $1.4 \pm 0.6$ [85] |
| Ho-$^3$He | 0.8 | $1.4 \pm 0.6$ [85] |
| Er-$^3$He | 0.8 | $1.4 \pm 0.6$ [85] |
| Tm-$^3$He | 0.8 | $1.5 \pm 0.6$ [85] |
| Th ($^3$F$_2$) -$^3$He | 0.8 | $0.96 \pm 0.35$ (Sect. 3.2.1) |
| Th ($^3$P$_0$) -$^3$He | 0.8 | $0.8 \pm 0.3$ (Sect. 3.5) |
| NH -$^3$He† | 0.7 | $2.7 \pm 0.8$ [59] |
| CaH-$^3$He | 0.4 | $1.5 \pm 0.6$ [86] |
| ThO (X, $\nu = 0$, J = 0)-$^3$He | 2.4 | $1.9 \pm 0.7$ (Sect. 4.2) |

### 2.1.2 Absolute cross section

The absolute value for the momentum-transfer cross section $\sigma_d$ has been measured in our lab in two ways. If the densities of the colliding partners are known, $\sigma_d$ can be determined from the re-equilibration time (i.e collision rate) after driving the system out of thermal equilibrium. For trapped atoms, the perturbation can be introduced by an optical pumping pulse and the atomic densities can be determined by absorption spectroscopy. This technique was applied to measure the Cr-Cr cross section [87]. For measuring atom-He cross sections, the perturbation is delivered by the initial laser ablation pulse and the re-equilibration time corresponds to the diffusion time. Helium density has been determined in three ways: a) filling the cell with a known amount of helium atoms [86] b) measuring the flow rate of the cell through a known conductance [88] c) measuring the pressure using a room temperature gauge and accounting for the $\sqrt{T}$ transpiration effect [89].

Once a primary atom-He cross section benchmark has been established, secondary calibrations can be determined by comparing diffusion time between the atom of interest and the benchmark atom (Tab. 2.1).

## 2.2 Trapping

For trapping to be accomplished one needs an energy minimum in free space. This can be done by applying an inhomogeneous electric, magnetic or optical field. Trapping field can be static or time-varying. Since Maxwell's equations do not allow for the creation of static, local electromagnetic field maximum [90], a static trap can only confine metastable low-field-seeking (LFS) state particles, which can decay to lower energy states during a collision. In contrast, this restriction does not apply to dy-

namic trap, which enables trapping in the absolute ground state (high-field-seeking). At sufficiently low temperatures, collisional loss of high-field-seeking states becomes energetically forbidden.

Any practical trapping technology can be characterized by both its trapping volume and trap depth. Trap depth is usually measured relative to the atoms' temperature.

$$\eta = \frac{\mathrm{U_{trap}}}{k_B T} = \frac{\max(\mathrm{U}) - \min(\mathrm{U})}{k_B T} \tag{2.11}$$

where $U(\vec{r})$ is the local potential energy. The atom density within the trapping volume is given by the Boltzmann distribution $n(\vec{r}) = e^{-U(\vec{r})/k_B T}$. Since any atoms reaching the edge are lost, the loss rate from a trapped sample is determined by the atomic flux ($f_A$) at the edge $f_A = A \cdot \nu \cdot \eta/4$. Therefore, loading is usually done at $\eta \gtrsim 10$ in order to achieve appreciable trap lifetimes [82].

In the buffer gas cooling experiments, we use only magnetic traps. For completeness, we discuss several other kinds of traps used in the field of cold atoms.

### 2.2.1 Optical dipole trap

An optical dipole trap exploits the A.C. Stark effect caused by a rapidly oscillating laser field. The operation principle relies on the difference scaling between trap depth and off-resonance excitation (which corresponds to heating) with respect to laser detuning $\delta$. For a two-level atom with transition strength and Rabi fequency $\Omega$, the resulting trap depth and heat rate are

$$\mathrm{U_{trap}} = \frac{\hbar \Omega^2}{4\delta}, \tag{2.12}$$

$$\Gamma_{\mathrm{heating}} = \frac{\Omega^2 \Gamma}{4\delta^2} \tag{2.13}$$

Because of the more rapid decay of heating rate than that of trap depth, the heating rate can be suppressed by choosing an appropriate laser detuning. Typically, 10 W of 1064 nm YAG or 100 W of 10.6 $\mu$m $CO_2$ laser light is focused onto a $(10\ \mu\text{m})^3$ volume, yielding a trap depth of $\sim 1$ mK [91]. Besides enabling the trapping of all ground-state sublevels, an optical dipole trap preserves the magnetic field as a free experimental parameter.

### 2.2.2 Electric trap

An electric trap depends on the Stark shift as a trapping mechanism. Because the nearest opposite parity state to the ground state of an atom is an electronic excited state, atoms exhibit quadratic Stark in any realizable laboratory field (up to 100 kV/cm). Assuming ground state polarizability of a few atomic units, the resulting trap is typically very shallow ($\sim 100\ \mu$K) [92]. Because of the availability of nearby, opposite parity rotational states, molecules are more readily polarizable (i.e., exhibit linear Stark shifts) and often have dipole moments as large as a few Debye. An A.C. electric trap with $\sim$10 mK trap depth and 1 $\text{mm}^3$ has been demonstrated with $ND_3$ [93] and OH [94].

### 2.2.3 Magnetostatic trap

Magnetic trapping relies on the Zeeman shift of atomic levels. For an atom with a magnetic moment $\mu$ in a B-field, the energy shift is given by

$$\Delta E = -\mu \cdot \mathbf{B} \tag{2.14}$$

The magnetic moment of an electron, approximately one Bohr magneton ($\mu_B$), sets the scale for the trap depths of atoms to be 0.67 K/T. Because of the prerequisite

cryogenic environment, superconducting magnetic coils are routinely used in buffer gas cooling. Using an anti-Helmholtz configuration, it is feasible to create a spherical quadrupole trapping field up to 4 T [95], which corresponds to a trap depth of 2.68 K for an alkali atom.

Buffer gas cooling produces atomic samples with initial temperatures of 200-300 mK using $^3$He or 600-800 mK using $^4$He (Fig. 2.1). In order to cool the atoms to a lower temperature, we must break the thermal contact between the atoms and the cell wall by removing the buffer gas.

During the process, the diffusive mean free path $\lambda_f$ of the atoms increases from a small fraction of the cell diameter to much greater. At high helium density (i.e. $\lambda_f$ is small), the atoms' lifetime is enhanced by the enforcement of diffusive motion. At low helium density, confinement of the atoms is provided the restoring force of the trapping potential. Inelastic collisions with helium to less trappable states shorten the atoms' lifetime [88].

Much of experimental effort has been devoted to the rapid removal of buffer gas after the initial cooling phase, including lowering the cell temperature [86, 96], or exposing a cryo-charcoal pump behind a valve [57, 82, 97]. It still takes $\sim 10-100$ ms to lower the buffer gas density from the loading requirement of $10^{16}$ cm$^{-3}$ to the long lifetime requirement of $10^{12}$ cm$^{-3}$. The ratio $\gamma$ of the momentum-transfer to Zeeman relaxation cross sections serves as a useful metric in determining the feasibility of loading a magnetic trap using buffer gas cooling. $\gamma$ can be thought of as the average number of collisions before relaxation. In general, a value of $\gamma \gtrsim 10^4$ is required.

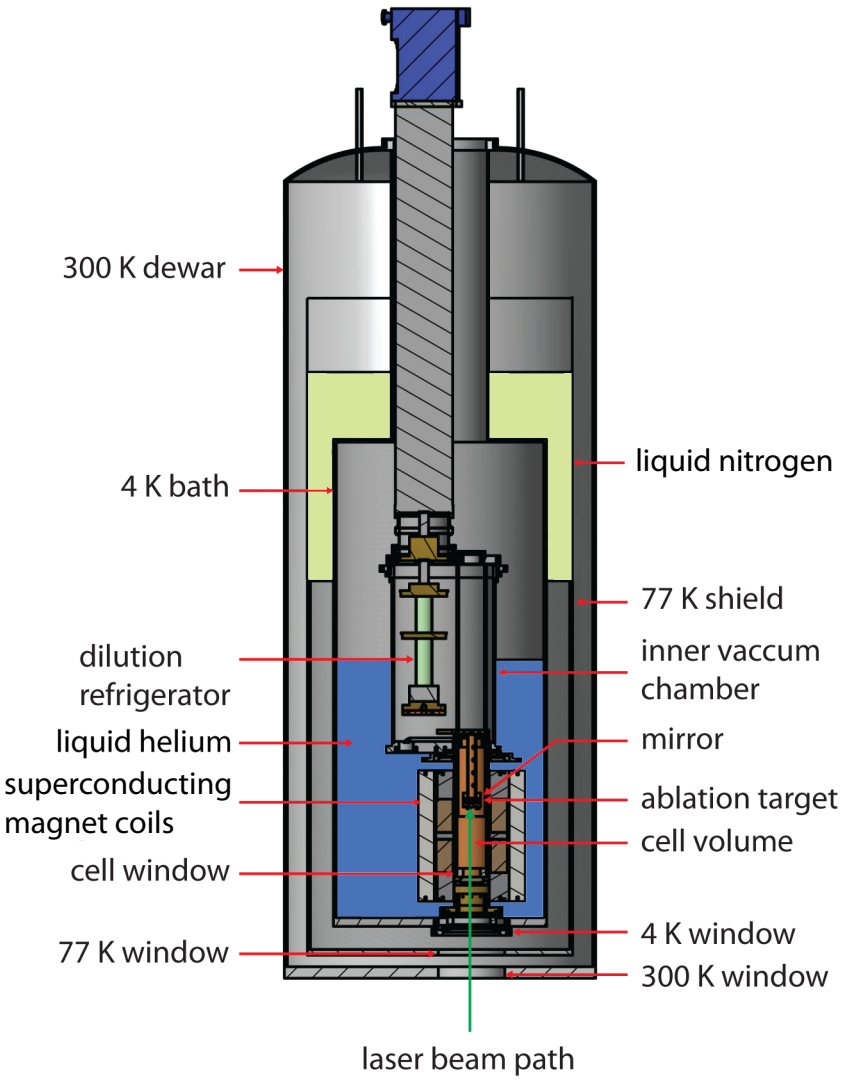


Figure 2.2: Schematics of the cryogenic apparatus.

## 2.3 Experimental design

The core of our apparatus (Fig. 2.2) consists of a cell below 1 K, which is cooled by a dilution refrigerator. The cooling power of the refrigerator limits the total heat load on the cell to be much less than 100 $\mu$W. Because of the mechanical delicacy of the refrigerator, the thermal anchoring is done via flexible heat links [71, 82, 86, 98]. Two types of cells, G-10 (fiberglass-epoxy composite) and copper, were used in our apparatus. Doubled-wall G-10 cells, which are cooled with a layer ($\sim$ 1 mm) of superfluid helium, permit rapid ramping of the magnetic field without heating due to eddy currents. Such a G-10 cell was used in the evaporative cooling of metastable helium [98]. The lower thermal conductivity of G-10 compared with copper in addition allows the introduction of short bursts ($\lesssim$ 1 ms) of helium gas via local heating, enabling loading of magnetic with atoms of low $\gamma \sim 10^4$ [71]. This property was exploited in our work with Tm and Er [66]. On the other hand, the excellent thermal conductivity of the copper cell leads to rapid thermalization and therefore allows measurements within $\sim$ 20 ms after a YAG ablation. It therefore provides an ideal environment for measuring inelastic collisions. The work described in this thesis utilized a copper cell. A hybrid approach, using a single-walled G-10 with copper wire among its length for thermal conductivity, was previously attempted. The hybrid cell was designed to minimize eddy current heating and thus (in principle) allow evaporative cooling [82]. However, its advantages over the doubled-wall G-10 cells have yet to be proven.

Surrounding the cell is a pair of superconducting coils, which can be connected in either the anti-Helmholtz configuration for trapping, or the Helmholtz configuration for Zeeman relaxation measurements. Since the lifetime of the trapped atoms

($\eta \lesssim 10$) depends exponentially on the cell radius [86], the clearance between the cell and the magnet bore is minimized to be just a few thousands of an inch. The magnet is submerged in liquid helium for cooling. The submersion is critical for dissipating the energy stored in the magnetic field when the superconductors quenches (i.e. going from superconducting to normal) [95]. Athough it is possible to build a deep superconducting magnet operating in vacuum [97], the presence of large amounts of copper used in that design precludes rapid ramping of the magnet field.

The requirement of submerging a magnet in liquid helium has led to considerable technical challenges with optical access. For each optical window, a flexible bellows is needed to expel the liquid helium from the beam path, along with black-body radiation shielding windows at 4 K, 77 K and 300 K, resulting in four additional vacuum seals. The flexibility provided by the bellows is required to prevent problems associated with mechanical overconstraints. Because of these requirements, our apparatus has only one window, although it would have been possible to add another orthogonal optical axis [99]. This single window is adequate for absorption spectroscopy, optical pumping [73] and even phase-contrast imaging [57], but fluorescence of the window caused by optical pumping limits diagonal fluorescent detection [71].

In order to monitor our atoms during our exploration of the periodic table in the past few years, we have adapted a wide range of laser technologies, including diode, titanium-sapphire, continuous-wave dye, pulsed dye lasers, over a broad spectral range (207 - 1092 nm). For the work describes in this thesis, only diode lasers were used for optical pumping and absorption detection (Fig. 2.3).

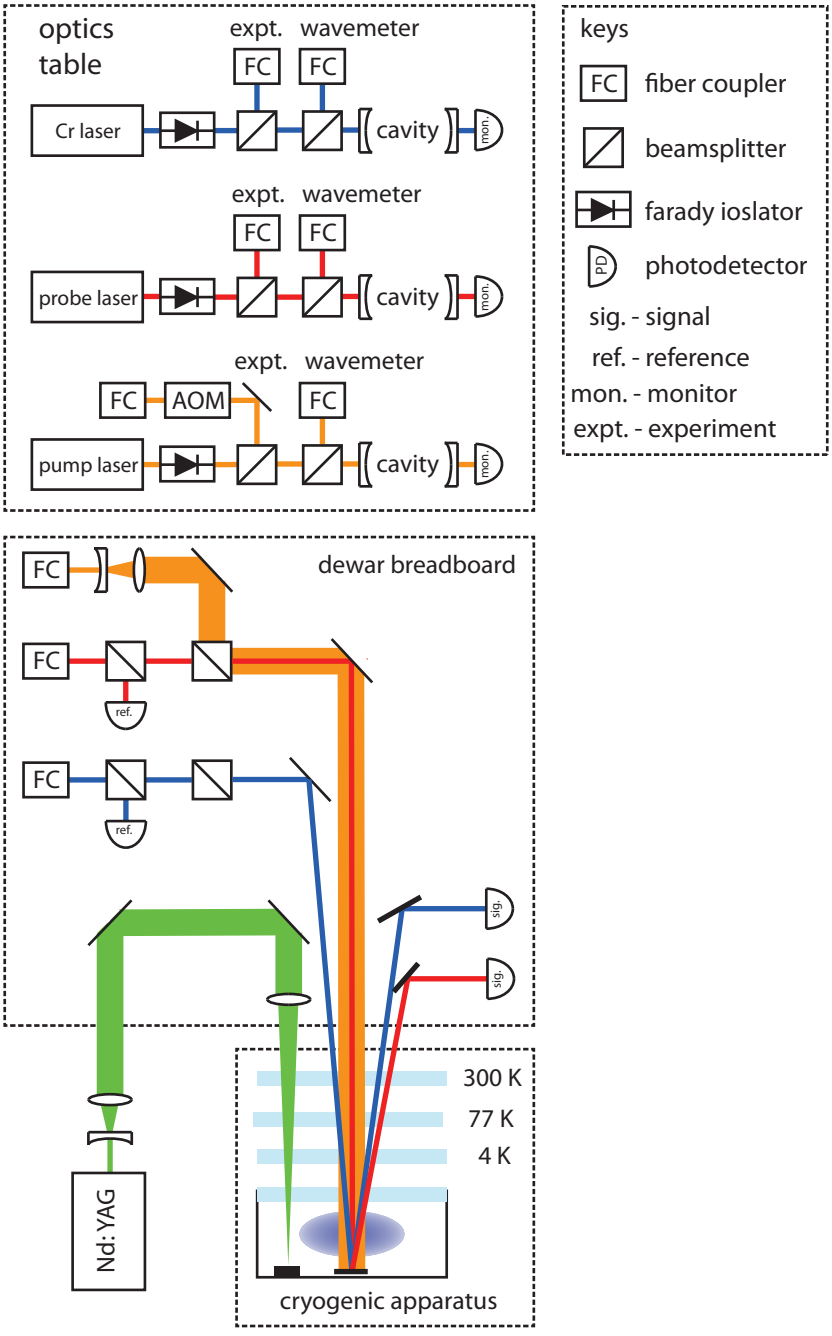


Figure 2.3: Schematics of the optics setup.

# Chapter 3

# Thorium-$^3$He collisions

This chapter describes measurements of inelastic collisions in the thorium-helium (Th-$^3$He) system. We study the Zeeman relaxation cross section in the ground $^3F_2$, in which interaction anisotropy is reduced by "submerged-shell" physics. We also explore the electronic quenching of the metastable first excited $^3P_0$ state. Although the stability of the $^3P_0$ state is not understood, de-excitation from $^3P_0$ to $^3F_2$ involves changing the electronic orbital angular momentum, and therefore, interaction anisotropy probably plays a role in the process.

## 3.1 Zeeman relaxation across the periodic table

Because it is a probe of low energy exchange in cold collisions and because of its implications to trapping, Zeeman relaxation is one of the most studied collisional processes in cold and ultracold systems across the periodic table. Due to the relatively simple, essentially structureless, electronic structure of the helium atom, atom-helium collisions are an important platform for understanding the mechanism of Zeeman relaxation, and provide useful links between theory and experiments. During a collision

between a paramagnetic atom and a helium atom, the Zeeman sublevel quantum number $m_J$ can change via the following mechanisms: electronic interaction anisotropy, spin-exchange and van der Waals (vdW) molecule formation.

As discussed in Ch. 2, the ratio $\gamma$ between the momentum transfer and the magnetic moment reorientation cross section, provides a useful metric to characterize inelastic collisions. $\gamma$ can be thought of as the average number of collisions before relaxation. In the simplest picture, an isotropic S-state atom (such as potassium) has a value of $\gamma > 10^8$ [68], compared with the anisotropic $^3P_2$-state of oxygen, which has $\gamma \sim 7$ [100]. The drastically different collisional properties can be explained by electronic interaction anisotropy.

Consider a collision between a paramagnetic atom and a helium atom mediated via the electrostatic interaction. In its ground $^1S_0$ state, a helium atom has a spherically symmetric electron distribution. If the colliding atom also has a perfect spherical electron distribution (e.g. another S-state atom), the classical electrostatic force is constrained by symmetry to be purely radial, and hence, cannot change the orientation of the magnetic moment. The symmetry in the interaction is broken if the paramagnetic atom (e.g. $^3P_2$) has an asymmetric electron cloud. In this case, the helium can apply a torque on the atom and drive a Zeeman relaxation. In quantum mechanics, Zeeman sublevels $m_J$ of a non-S state atom correspond to different projections of the magnetic quantization onto the collision axis. Anisotropy in interaction lifts the degeneracy between $m_J$ states, causing differential phase-shifts among the incoming and outgoing quantum states, and thus changing the Zeeman $m_J$ states in the process [84].

For a spherically symmetric paramagnetic atom, Zeeman relaxation is driven by a diverse set of mechanisms. For collisions between an S-state alkaline atom and

$^3$He, Zeeman relaxation is caused by spin-exchange via the hyperfine interaction $\mathrm{I_{hf}}$. Intuitively, the strength of the interaction is proportional to the wavefunction overlap between the alkaline valence electron and the $^3$He nucleus.

$$\mathrm{I_{hf}} = |\eta\phi(R)|^2 \tag{3.1}$$

where $\eta$ is the alkaline atom specific enhancement factor and $\phi(R)$ is the wavefunction of the alkaline valence electron at the $^3$He nucleus. Spin-exchange is generally slow, with rate constant $k_{se} \sim 10^{-22}$ cm$^3$s$^{-1}$ at 1 K [68].

An atom in the nitrogen column has a nominally $^4\mathrm{S}_{3/2}$ ground state, but its S-state character can be significantly perturbed by relativistic spin-orbit interaction, i.e. the ground state electron cloud can be asymmetric. The anisotropic static dipole polarizability scales roughly with the nuclear charge $Z$ as $Z^4$, and Zeeman relaxation is expected to be more rapid among the heaviest atoms in the column. For example, Bi has only $\sim 57\%$ S character [101] and the nominally S-state Sb atom behaves very differently from an S-state atom, with $\gamma \sim 1000$ at T=800 mK and B $\sim 1$ T [72].

For a atom in the Boron column, its ground state ($^2\mathrm{P}_{1/2}$) can be expressed in the $l_m, m_s$ bases:

$$\left|J=\frac{1}{2}, s=\frac{1}{2}\right\rangle = \sqrt{\frac{2}{3}}\left|l_m=0, m_s=\frac{1}{2}\right\rangle + \sqrt{\frac{1}{3}}\left|l_m=1, m_s=-\frac{1}{2}\right\rangle \tag{3.2}$$

The first (second) term corresponds to a equal mixture of the $p_x$ and $p_y$ ($p_z$) orbitals. Ignoring the electron spin, the $^2\mathrm{P}_{1/2}$ state consists of equal portion of each $p_x, p_y$, and $p_z$ and is therefore spherically symmetric.

For an atom in Boron column, the spherical symmetry of the electron distribution is perturbed by mixing of fine-structure states ($^2\mathrm{P}_{3/2}$) during a collision. The energy splittings between these states are determined by the spin-orbiting coupling $\Delta_{SO}$, and therefore, the Zeeman sublevel $m_J$-changing collisions are suppressed with higher

$\Delta_{SO}$. Because of their larger $\Delta_{SO}$, heavier members of the column are expected to be less susceptible to Zeeman relaxation, in contrast to the opposite trend of the nitrogren column. Direct comparisons have recently been made between theory and experiments. This theory is expected to be applicable to the metastable $^2P_{3/2}$ in the halogen column [73, 102].

A different and interesting pathway to rapid Zeeman relaxation for an S-state atom is the formation of van der Waals (vdW) molecules. The weak vdW interaction between most paramagnetic atoms and helium can support bound states with a few kelvin of binding energy $E_b$ [69]. $E_b$ tends to be stronger for heavier atoms. vdW molecules open additional relaxation channels such as the spin-rotation interaction, chemical exchange and collision-induced vdW molecule dissociation, though the amount of each contribution is very atom specific. Because of the extra rotational degree of freedom in the vdW molecule, level-crossings of the different rotational levels are now possible, causing faster trap loss through Majorana-type processes at finite magnetic field [69].

For most non-S state transition metals and lanthanides, outer s-orbitals are occupied before the valence d- and f-orbitals are filled. During a cold collision with helium, the outer s-electrons limit the atom-atom separation, "shielding" the electrostatic anisotropy of the d- and f-shells. Such atoms are said to have a "submerged-shell." There is a huge variation of inelastic suppression factors due to the effect across the period table, ranging from a factor of 200 for titanium [63] to over $10^4$ for the lanthanides [64]. The "submerged-shell" model can also be extended to understand fine-structure J-changing collisions with helium [103], but it has limited applications to collisions between two "submerged-shell" atoms [66, 67, 104], due to their stronger interaction.

This chapter describes an experiment using atomic thorium to study the effects of possible shielding in the actinides, the first study of its kind. In doing so, we provide quantitative comparison of the degree of outer s-electron shielding between 3d4s (e.g. Ti), 4f6s (e.g. Tm) and 6d7s (e.g. Th) systems. This work will complete the overview of Zeeman relaxation across the periodic table. A value of $\gamma \gtrsim 10^4$, if found, could lead to magnetic trapping of the actinides using buffer gas cooling. However, we find a much smaller value of $\gamma \sim 500$ for thorium.

## 3.2 Experimental setup

The core experimental approach to all of our work is the creation of cold, dilute gases of Th in the presence of cold $^3$He gas. We prepare cold samples of atomic thorium ($> 10^{11}$) at 800 mK. Our setup consists of a copper cell at 800 mK, cooled by a dilution refrigerator via a flexible heat link (Sect. 2.3). A pair of superconducting Helmholtz coils creates a uniform magnetic field over the cell region for Zeeman relaxation measurements. No magnetic field is applied in the experiments on the metastable excited $^3P_0$ state of thorium. Rather, the $^3P_0$-state experiment probes the translational-to-electronic energy transfer, as described in Sect. 3.4.

Atomic thorium is introduced into the buffer gas via laser ablation of a solid thorium metal target. Thorium atoms thermalize to the cell temperature via collisions with $^3$He before diffusing to the cell wall, where they stick and can no longer be studied. We measure the atoms' temperature by fitting a Voigt profile to the optical absorption spectrum (Fig.3.1) of the $6d^27s^2$ ($^3F_2$) $\rightarrow$ $6d^27s7p$ ($^3G_3$) transition at 372 nm. Our measurements were taken at long enough times after ablation such that only the lowest order diffision mode needed to be considered. The signature of single diffusion mode is a single exponential decay of the thorium optical density [86]. In

this case, the diffusion time constant $\tau_d$ in a cylindrical cell of radius $r$ and length $L$ is given by

$$\tau_d = \frac{n_b \sigma_d}{G\bar{v}}, \tag{3.3}$$

$$G = \frac{3\pi}{32}\left(\frac{j_{01}^2}{r^2} + \frac{\pi^2}{L^2}\right), \tag{3.4}$$

where $n_b$ is the buffer gas density, $\sigma_d$ is the thermally averaged momentum transfer cross section, $G$ is the cell's geometric factor, $j_{01} \approx 2.4$ is the first zero of the Bessel function $J_0$, and $\bar{v}$ is the mean Th-$^3$He center of mass speed [81].

### 3.2.1 Helium density calibration

To calibrate the absolute density of $^3$He, we simultaneously ablate a piece of chromium metal and measure the atomic chromium's "late" diffusion time of the lowest diffusion mode by monitoring its absorption signal via the $3d^5(6S)\ 4s\ (a\ ^7S_3) \rightarrow 3d^5(6S)\ 4p\ (z\ ^7P_4)$ transition at 426 nm. We use $\sigma_d = 1.1 \times 10^{-14}$ cm$^2$ for the Cr-$^3$He diffusion cross section [86]. From the ratio of the diffusion time, we determine for Th ($^3F_2$) -$^3$He $\sigma_d = (9.6 \pm 3.5) \times 10^{-15}$ cm$^2$.

## 3.3 Zeeman relaxation in the ground state

To measure Zeeman relaxation, we apply a uniform magnetic field of up to 2 T to spectroscopically resolve the Zeeman sublevels ($m_J$) of the thorium ground $^3F_2$ state, which we probe using absorption spectroscopy on the 372-nm transition. We drive the system away from thermal equilibrium and then monitor repopulation from other Zeeman sublevels via inelastic collisions. Here we deplete a high-field-seeking (HFS) $m_J > 0$ state via an optical pumping pulse using the $6d^27s^2$ ($^3F_2$) $\rightarrow$ $6d^27s7p$ ($^3D_1$) transition at 380 nm, as shown in Fig. 3.3.

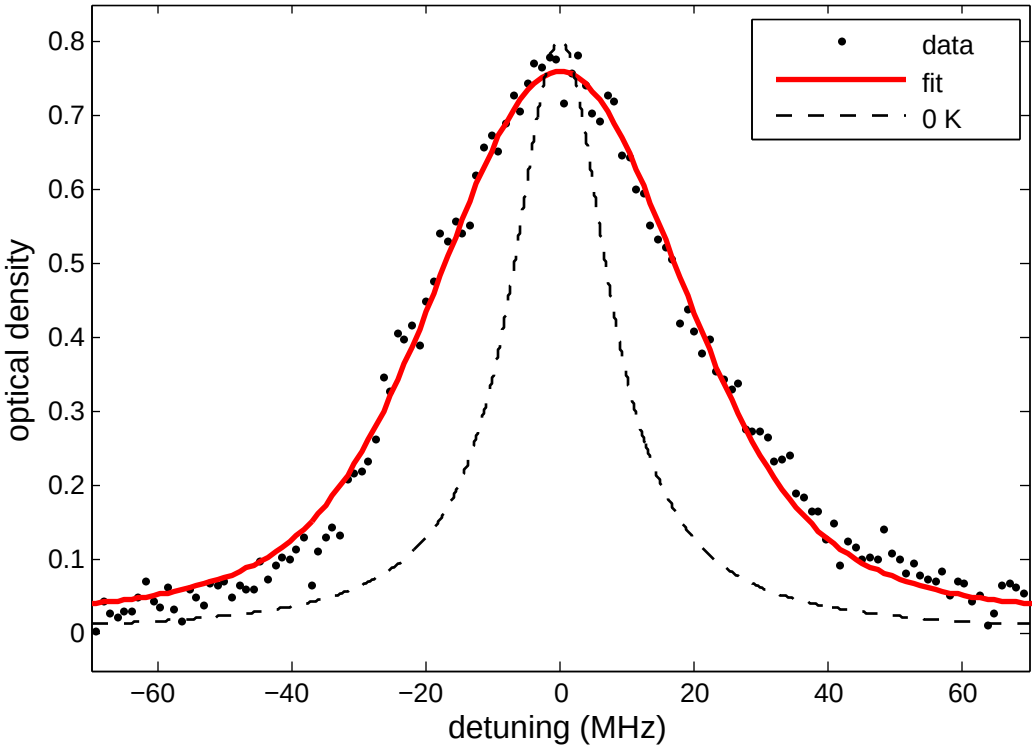


Figure 3.1: Doppler profile of thorium probed using the $6d^27s^2$ ($^3F_2$) $\rightarrow$ $6d^27s7p$ ($^3G_3$) transition at 372 nm. The temperature ($800 \pm 100$) mK, obtained from fitting the spectrum to a Voigt lineshape is consistent with the cell temperature read from a thermistor.

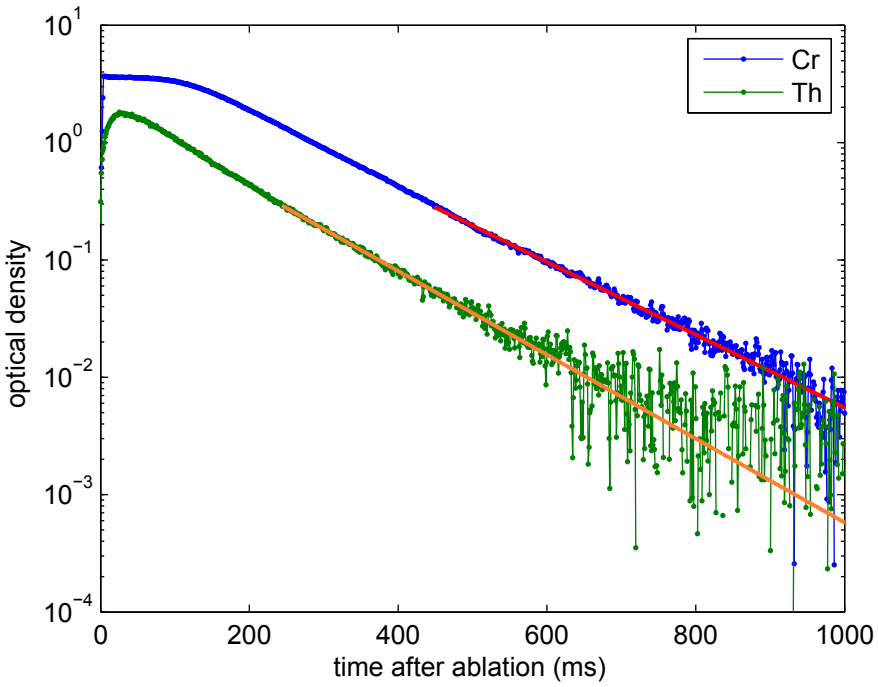


Figure 3.2: Simultaneous production and cooling of atomic Th and Cr. From the ratio of the diffusion time, we determine for Th ($^3F_2$) -$^3$He $\sigma_d = (9.6\pm3.5)\times10^{-15}$ cm$^2$.

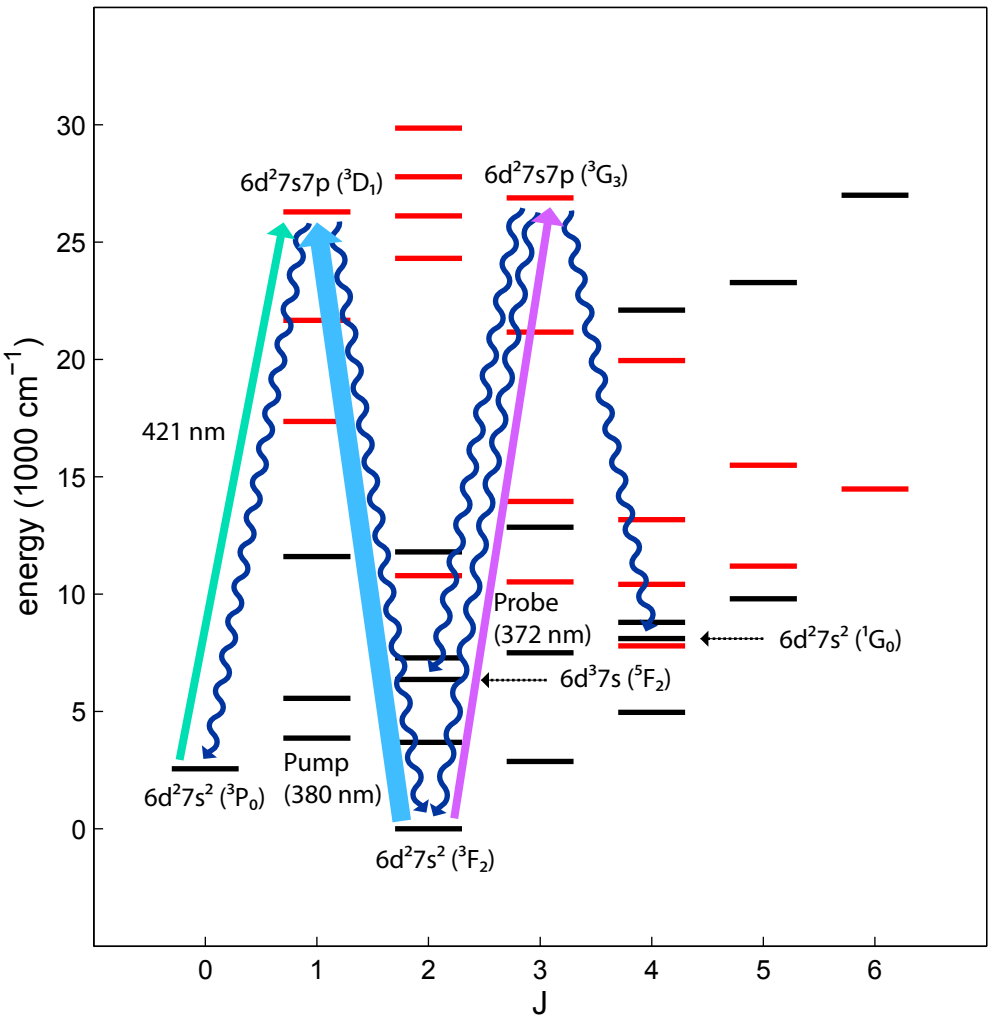


Figure 3.3: Energy levels of thorium up to 30 000 cm$^{-1}$ [105]. Black (red) line indicates parity even (odd) state. In Zeeman relaxation measurement, the ground $^3$F$_2$ state is pumped by the 6d$^2$7s$^2$ ($^3$F$_2$) $\rightarrow$ 6d$^2$7s7p ($^3$D$_1$) transition at 380 nm and probed by the 6d$^2$7s$^2$ ($^3$F$_2$) $\rightarrow$ 6d$^2$7s7p ($^3$G$_3$) transition at 372 nm. In the excited $^3$P$_0$ measurements, the state is populated by optical pumping via 6d$^2$7s7p ($^3$D$_1$) and is probed by 6d$^2$7s$^2$ ($^3$P$_0$) $\rightarrow$ 6d$^2$7s7p ($^3$D$_1$) transition at 421 nm.

Table 3.1: Some of the measured g-factors that are different from their values calculated using spectroscopic term assignments (Eq. 3.5). We use the literature value [106] for the ground state's g-factor and deduce g-factors of the excited states from the observed Zeeman shifts. The frequency shifts were measured using a wavemeter. The uncertainty in $g_J$ is dominated by current-to-field calibration of the coils.

| level ($cm^{-1}$) | term | $g_J$ (calculated) | $g_J$ (observed) |
|---|---|---|---|
| 0 | $^3F_2$ | 0.667 | 0.736 [106] |
| 26 287.049 | $^3D_1$ | 0.5 | $0.9 \pm 0.05$ (this work) |
| 26 878.162 | $^3G_3$ | 0.75 | $1.1 \pm 0.05$ (this work) |

### 3.3.1 g-factors

The expected Zeeman shift of an atomic transition can be calculated from the Landé g-factors, $g_J$, of the terms of the lower and the upper states using Eq. 3.5.

$$g_J = \frac{3}{2} + \frac{S(S+1) - L(L+1)}{2J(J+1)} \tag{3.5}$$

if both $L$ and $S$ are good quantum numbers for the states.

The literature value for Th ($^3F_2$) is $g_J = 0.736$ [106], compared to $g_J = 2/3$ predicted by Eq. 3.5. The discrepancy is not unexpected for heavy atoms, and it suggests a significant relativistic perturbation to the atomic states, which can be of importance to the cold collisional properties [101]. We adopt the literature value for the ground state $g_J$, and account for the difference between the calculated and the measured Zeeman shifts as observed values for the excited states $g_J$ (Tab. 3.1).

### 3.3.2 Optical pumping

The method used here for measuring the cross section ratio $\gamma$, i.e. by observing the recovery of HFS states, is different from that used in [107], which relies on monitoring

the decay of a low-field-seeking (LFS) state populated during the initial laser ablation. In the latter case, measurements made soon after ablation are complicated by high-order diffusion modes and thermal effects from the laser ablation. Relying only on late-time data to avoid these effects limits the sensitivity of that method to $\gamma \gtrsim 1000$ [71].

In this work, the use of optical pumping to drive the system out of equilibrium allows us to perform the measurements after the decay of high-order diffusion modes and the establishment of thermal stabilization of the cell, while preserving sensitivity to short time scales (i.e. low $\gamma$). The observation of a simple exponential decay of atomic optical density during the measurements confirms that no other processes interfere with simple Zeeman relaxation . This method thus theoretically enables a measurement of $\gamma$ to values as low as $\approx 1$. Additionally, using optical pumping not only allows a higher data rate by enabling repetition of relaxation measurements within an atom production (see Fig. 3.4), but also provides a robust systematic check if we ensure the measured value is independent of time delay from initial atom production [73, 104].

### 3.3.3 Results and analysis

The observed time constant $\tau_Z$ for the repopulation of the HFS state via inelastic collisions is given by [72]

$$\tau_Z = \frac{\gamma}{\bar{v}^2 G \tau_d} \tag{3.6}$$

where $G$ is the cell's geometric factor (Eq. 3.4) and $\bar{v}$ is the mean center of mass speed.

As shown in Fig. 3.5, the measured dependence of the recovery time of the HFS state on its diffusion time agrees with Eq. 3.6, where the value for $\gamma$ can be extracted

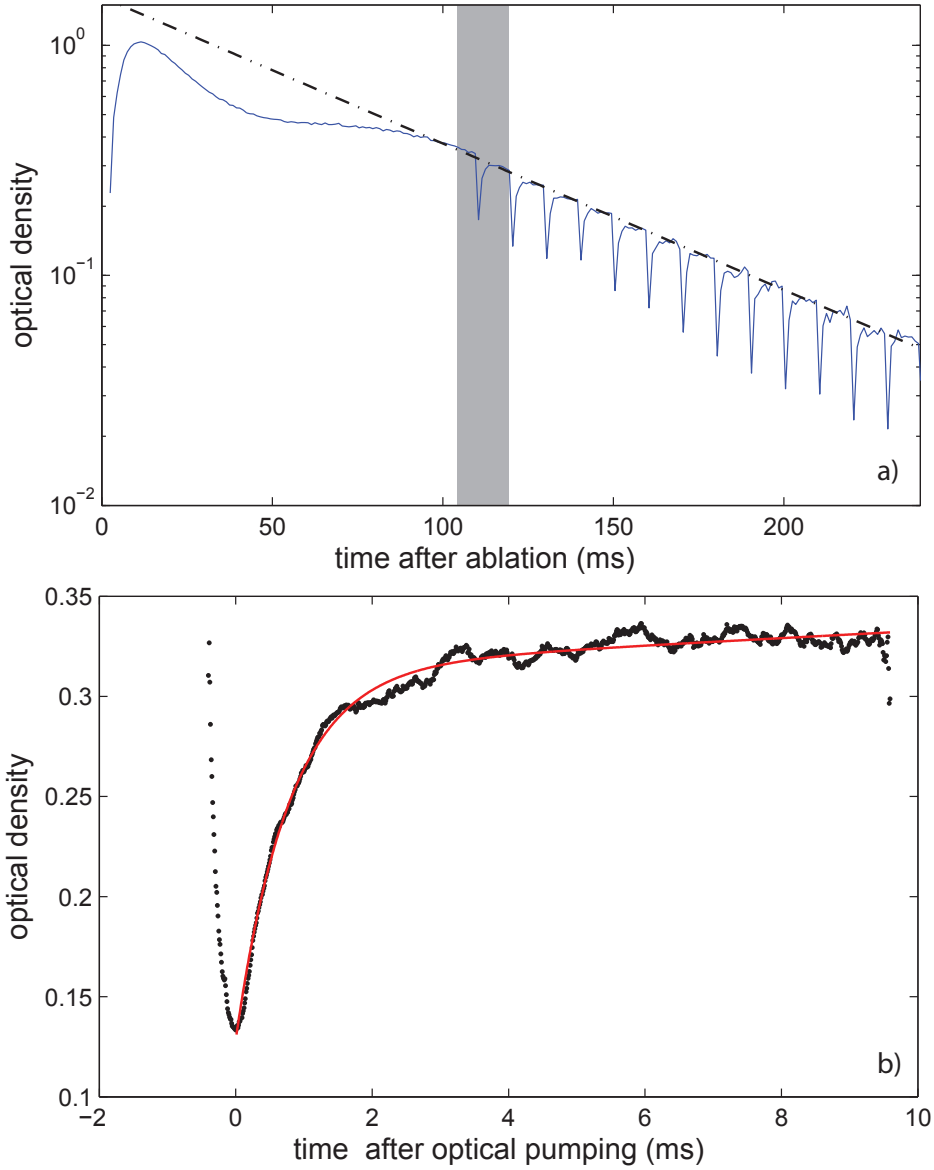


Figure 3.4: (a) The optical density (OD) of atomic thorium during a Zeeman relaxation measurement. Measurements are performed starting 100 ms after ablation, when both diffusion modes and temperature are stabilized, as verified by the observation of a simple exponential decay of the atomic OD (dashed-line). The plot shown in (b) corresponds to the shaded area in (a) after subtraction of the diffusive baseline, and shows the depletion of OD by optical pumping and recovery of OD via inelastic collisions. Multiple measurements are made with separate optical pumping pulses before the atoms diffuse to the cell wall.

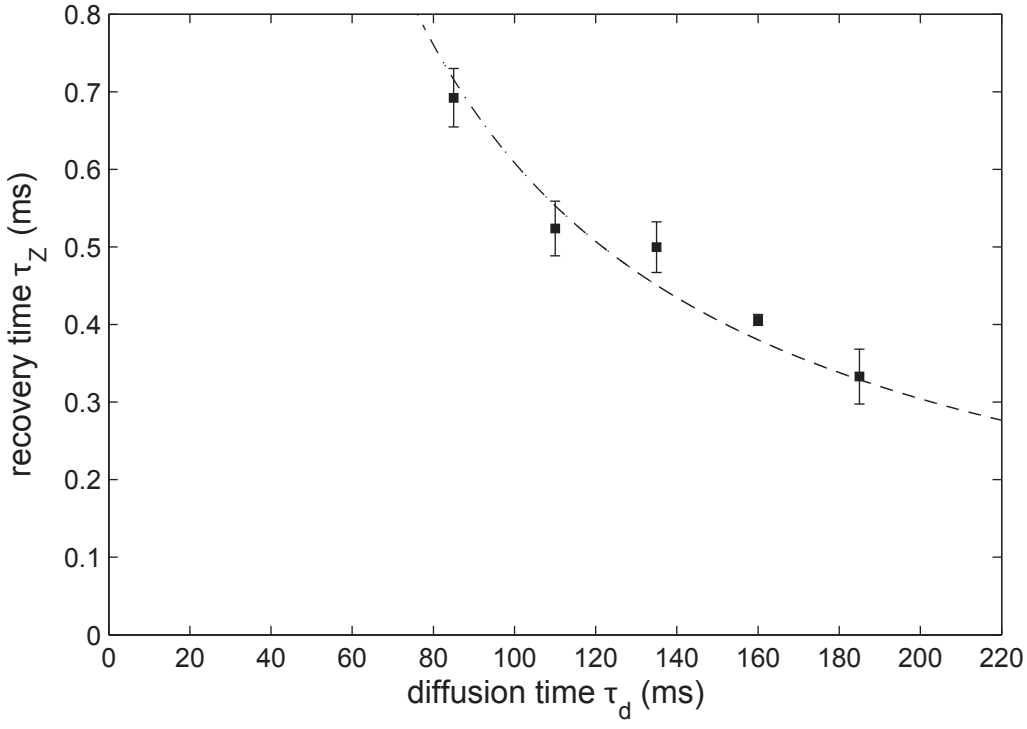


Figure 3.5: Zeeman relaxation measurement. Fitted repopulation time $\tau_Z$ of the most high-field seeking (HFS) state ($m_J = J$) of atomic thorium at different $^3$He densities ($\tau_d \propto n_{\mathrm{He}}$) in a 0.5 T magnetic field. Error bars are statistical uncertainties. The ratio $\gamma$ of the momentum-transfer to Zeeman relaxation cross section is given by fitting to Eq. 3.6.

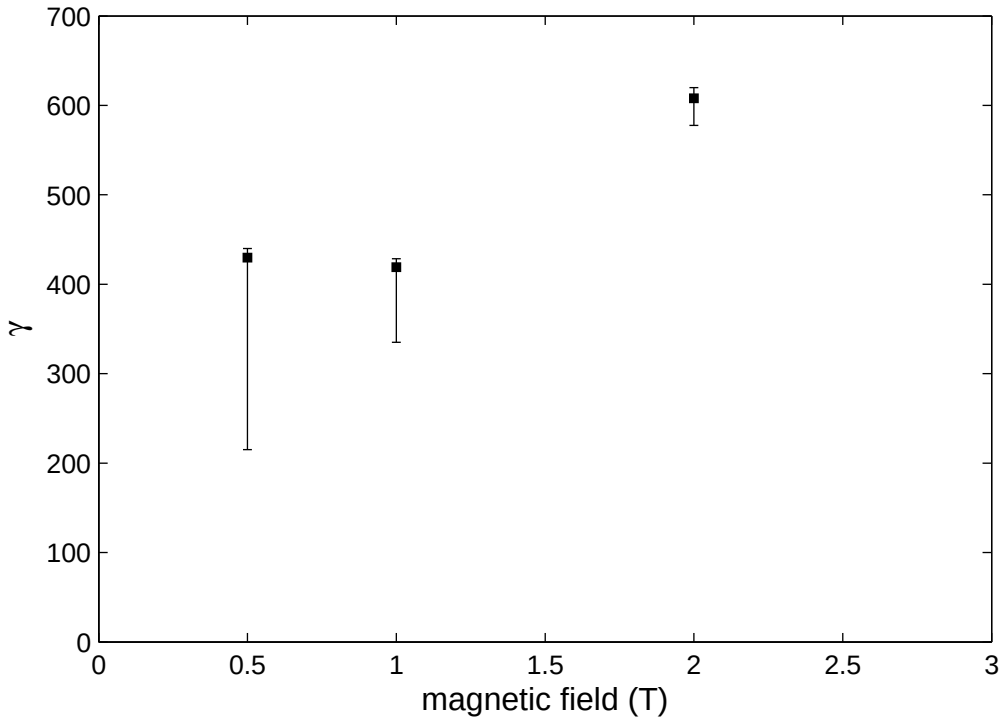


Figure 3.6: Momentum-transfer-to-Zeeman-relaxation collision ratio $\gamma$ for Th ($^3F_2$) ground state measured at 800 mK. The upper limit of the error bars is statistical uncertainty from fitting, while the lower limit represents uncertainty caused by thermal excitations.

as a fit parameter.

At finite temperature, an inelastic collision can sometimes have sufficient energy to promote a thorium atom from the stretched HFS state to higher sublevels, slowing the relaxation to equilibrium and resulting in an overestimation of $\gamma$. We simulated our system using the model developed in [107]. In Fig. 3.6, the upper limit of the error bars is statistical uncertainty from fitting, while the lower limit represents systematic error due to such thermal excitations.

We also repeat the Zeeman relaxation measurement on the ground-state sublevel with $m_J = J - 1$ at 0.5 T, and found $\gamma$ to be statistically similar to that of the most HFS state ($m_J = J$). We could not make this comparison at higher magnetic field due to insufficient thermal population of the $m_J = J - 1$ state.

A source of possible measurement error is the filling of the HFS state from long-lived states (e.g. $^5F_2$. see Fig. 3.3) populated during optical pumping due to nonzero branching from the excited $^3D_1$ state. The state lifetimes and transition strengths are not sufficiently known [105] to quantify the populations of other excited states or the rate of decay into the ground state. However, the populations in such states due to optical pumping will depend sensitively on both power and duration of the pump and probe lasers. We change these parameters by a factor of 2 and obtain a statistically equivalent values of $\gamma$. Therefore we conclude that decay from other states does not affect our measurement with the experiment resolution.

We find that $\gamma \approx 500$, which is too small for loading atomic thorium into a magnetic trap in our experiment (Sect. 2.2.3).

## 3.4 Excited state atomic collisions

In addition to our study of anistropy in the ground state, we also explored the collisional properties of the first excited $^3P_0$ state in thorium. In contrast to previous studies of metastable $^3P_J$ states in alkaline earths [108–110], transitions between fine structure multiplets are not energetically allowed. This permits a direct study of metastable electronic quenching. We were also able to determine that this metastable state has a very long lifetime, and is apparently not strongly affected by the perturbations in this complex, heavy atom.

## 3.5 Collisions in the excited $^3P_0$ state

We also apply the optical pump and probe technique to study collisions in the metastable first excited $^3P_0$ state of atomic thorium. The state is probed using the $6d^27s^2$ ($^3P_0$) $\rightarrow$ $6d^27s7p$ ($^3D_1$) transition at 421 nm. When the thorium gas is produced via laser ablation, a few percent (optical density $\sim$0.01) is populated in the $^3P_0$ state. We increase the state population by an order of magnitude using optical pumping via the $6d^27s7p$ ($^3D_1$) state (see Fig. 3.3 and Fig. 3.7). We measure the relaxation time of the $^3P_0$ state at various buffer gas densities to search for collisional quenching of the excited state.

### 3.5.1 Results and analysis

The results for the $^3P_0$ state are shown in Fig. 3.8. The excited state lifetime $\tau_P$ shows a linear dependence on the ground state ($^3F_2$) diffusion time $\tau_F$, which is proportional to the buffer gas density. The lifetime $\tau_P$ is determined by five effects: refilling from

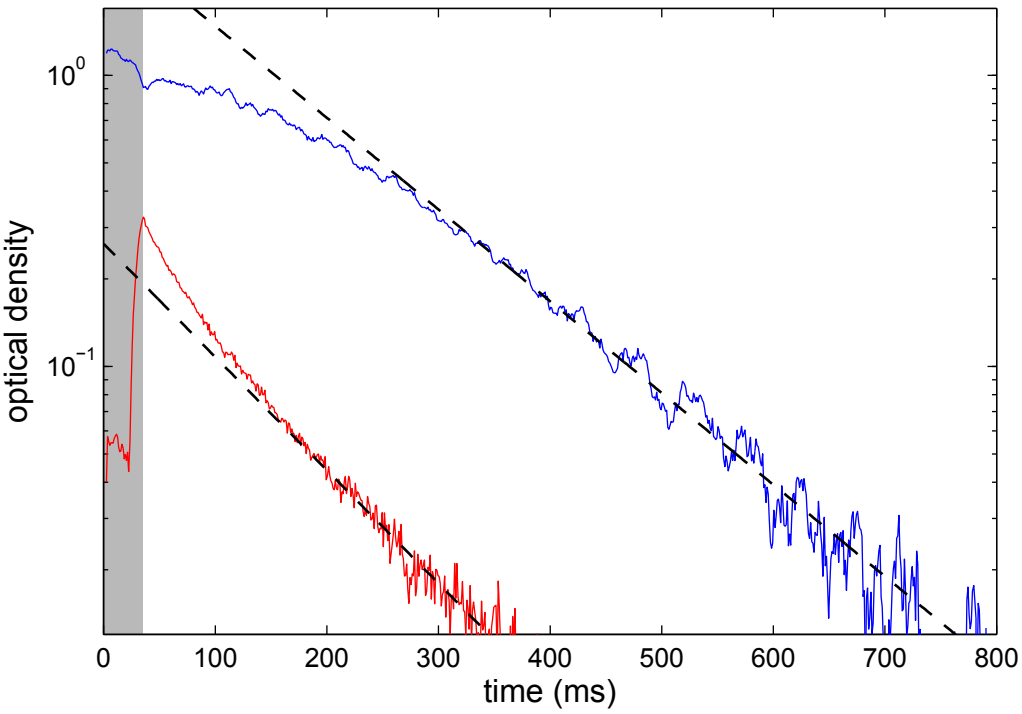


Figure 3.7: The optical density (OD) of atomic thorium during the excited $^3P_0$ state measurement. Blue (red) is the OD of the $^3F_2$ ($^3P_0$) state. Optical pumping is applied in the first 20 ms (shaded area) to transfer population from the ground $^3F_2$ state to the excited $^3P_0$ state. Dashed lines are single-exponential fits to the lowest diffusion mode at late times. Diffusive fits start at 310 ms and 180 ms for the $^3P_0$ and the $^3F_2$ state respectively.

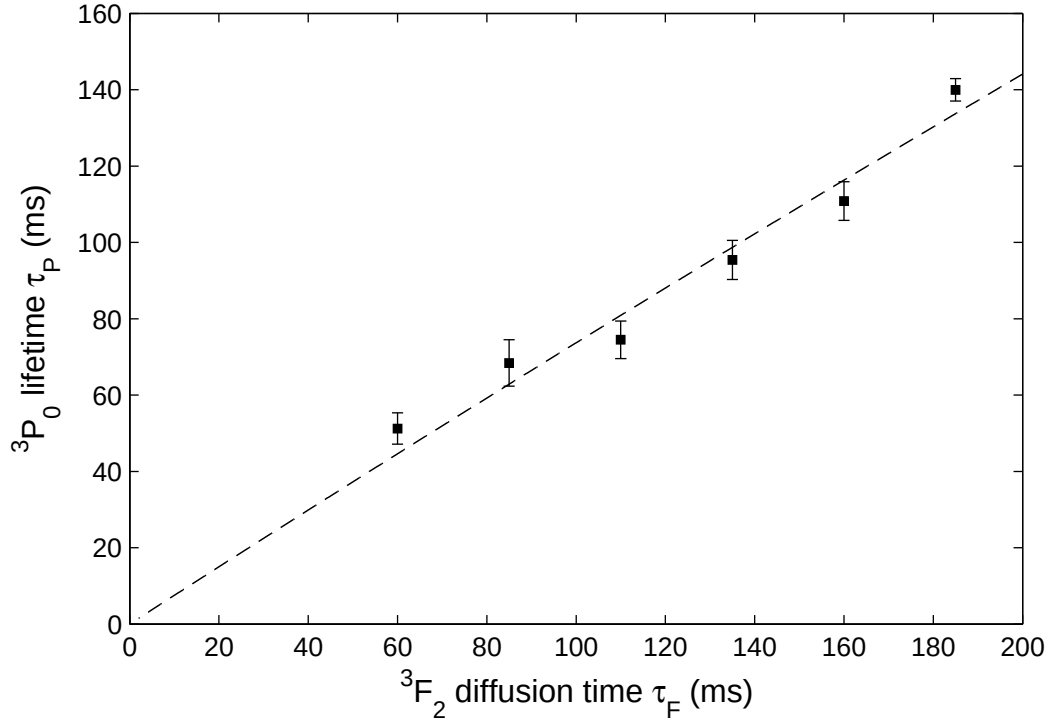


Figure 3.8: Linear dependence of the excited $^3P_0$ state lifetime $\tau_P$ on diffusion time and buffer gas density.

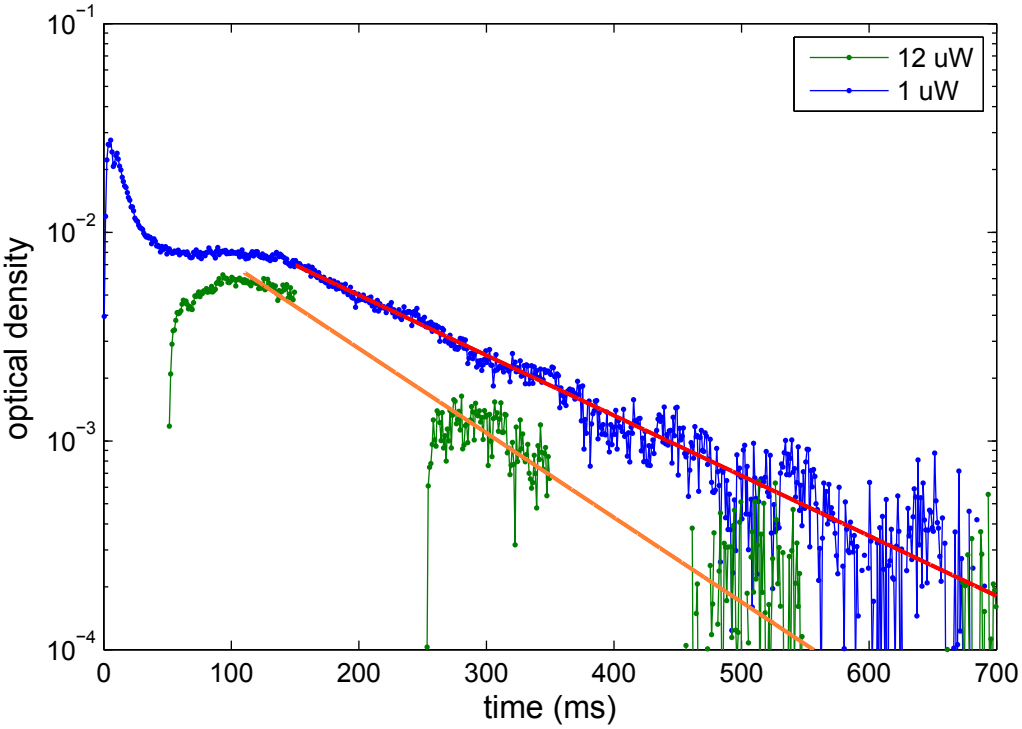


Figure 3.9: At 12 $\mu$W probe laser power, the excited state lifetime $\tau_P$ is determined by optical pumping instead of diffusion or radiative decay. The absence of recovery of the $^3$P$_0$ population suggests the effect on $\tau_P$ by refilling from upper states is insignificant.

a reservoir, optical pumping, diffusion, collisional quenching and radiative decay.

We first consider the possibility that the $^3$P$_0$ state is constantly refilled by populations from reservoir states with higher energies, the only mechanism of the four that can increase the observed value of $\tau_P$. We probe the $^3$P$_0$ state with sufficient laser power so that $\tau_P$ is determined by optical pumping instead of diffusion or radiative decay. We shutter the probe beam for 100 ms before probing the state again. We do not observe a recovery of the $^3$P$_0$ population (Fig. 3.9), and thus we conclude that contributions to $\tau_P$ by refilling from a reservoir is insignificant.

Detector efficiency limits our probe laser power to be greater than 150 nW. We observe a negatively correlated, power dependent slope. We do not have sufficient

data to eliminate the effect on $\tau_P$ imposed by optical pumping by extrapolating to zero probe power.

The laser-independent component of the slope (in Fig. 3.8) is determined by the ratio for the elastic cross-section between Th ($^3$P$_0$)-$^3$He and Th ($^3$F$_2$)-$^3$He (i.e. diffusion).

Finally, collisional quenching causes a negative slope and radiative decay imposes a $^3$He density ($\tau_F \propto n_{\mathrm{He}}$) upper limit on $\tau_P$. Although we do not separate the contribution to the slope by optical pumping and diffusion, the linear dependence (with a positive slope) of $\tau_P$ on $\tau_F$ enable us to conclude that no electronic quenching collisions were observed. Using the highest buffer gas density data point, we can set bounds of $\gamma > 10^6$ and $\tau_R > 134$ ms with 95% confidence, where $\tau_R$ is the radiative lifetime of the excited state.

## 3.6 Summary and future outlook

In this Chapter, we have examined anisotropy reduction by "submerged-shell" physics among the actinides. We measure the ratio $\gamma$ of the momentum-transfer to the magnetic reorientation cross sections of thorium in the ground $^3$F$_2$ state. We find that $\gamma \approx 500$, which is well above that of open-shell oxygen, but well below that of "submerged-shell" lanthanides. This value of $\gamma$ is too small for direct buffer gas loading into a magnetic trap (Sect. 2.2.3), but it is sufficient for indirect loading from a buffer gas beam [111]. This brings the possibility of studying trapped, cold atomic thorium.

Although atomic thorium is a good starting point to study "submerged-shell" physics among the actinides, it is one of the only two elements, along with actinium, in the series with an unfilled 5f shell. It would be instructive to measure the Zeeman

relaxation in other elements, such protactinium and uranium. Since the rest of the row consists of artificially prepared elements, it may be difficult to obtain samples with sufficient quantity to study. Trapping of Americium would be very interesting from collisional physicists' point of view: Competing relativistic effects can both increase anisotropy by mixing in exciting state (e.g. Bi) and decrease anisotropy by shielding, in addition to driving Zeeman relaxation via van der Waals' complex formation.

We also study metastable Th, setting a lower bound of $\gamma > 10^6$ for electronic quenching of the first excited $^3P_0$ state. This very low quenching cross section allows for the determination of a long radiative lifetime for Th ($^3P_0$) of $\tau > 134$ ms. This invites the possibility of studying ultracold metastable Th in an optical lattice, as was done with the lanthanide Yb [112].

Together with the unexplained results of collisions between Yb atoms in $^3P_0$ states [112], there may be a general trend of robustness in the excited $^3P_0$ state, opening up new opportunities for applications using metastable atoms.

A natural extension to the study of excited state collisions is to explore the metastable $^2P_{1/2}$ states in the halogens [71, 102]. Although recent experiments with Ga, In [102] and Al [73] have confirmed the slow Zeeman rate of the $^2P_{1/2}$ state, the prediction of the metastable halogens' stability against electronic quenching remains untested. If the theory is confirmed, it could open up a new column of atoms for trapping. The successful integration of a gas injection line with our dilution refrigerator for the NH work (for introducing $H_2$ and $N_2$ ice) could provide an ideal launchpad for such work.

# Chapter 4

# Thorium Monoxide-$^3$He collisions

This chapter describes measurements of inelastic collisions in the thorium monoxide-helium (ThO-$^3$He) system. We observe indirect evidence for ThO-He van der Waals (vdW) complex formation via 3-body recombination. We also explore the translational-to-vibrational energy transfer in the X ($\nu = 1$) state. Because interaction potentials generally have weak functional dependence on internuclear separation compared to the angular anisotropy, vibrational quenching is expected to be slow in comparison to rotational quenching [83]. Our results are consistent with this expectation. In our system, since vibrational quenching is much faster than the time to thermal equilibrium between free and vdW bounded ThO molecules, vdW complex plays only a limited role in the vibrational quenching process. Finally, we study translational-to-electronic energy transfer in the H ($\nu = 0$) excited states, and we find the process to be slow.

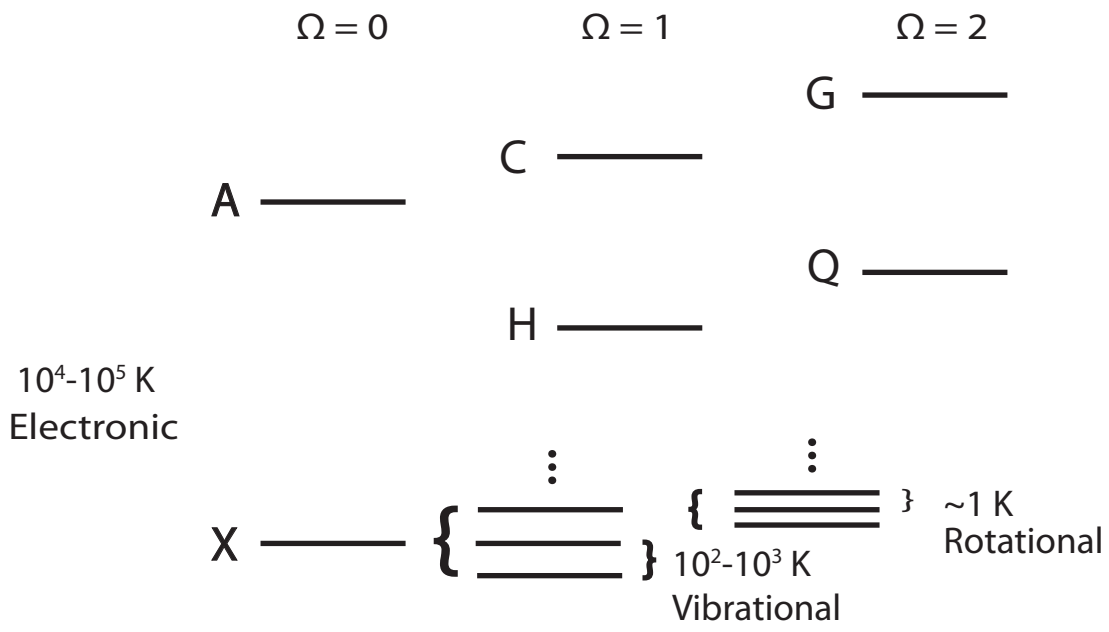


Figure 4.1: Energy level hierarchy of the ThO molecule, showing electronic, vibrational and rotational degrees of freedom, which are separated by a few orders of magnitudes in energy. $\Omega$ refers to the projection of total electronic angular momentum (electronic orbital $L$ and spin $S$) on the internuclear axis.

## 4.1 Inelastic collisions between molecules

The full potential of molecules for applications in physics will only be realized by exploiting their additional internal degrees of freedom (DOF) i.e. rotational and vibrational states (Fig.4.1). Rotational states could be efficiently coupled to solid-state devices via microwave radiation [33], while vibrational states could provide sensitive tests for variation in the proton-to-electron mass ratio [113]. Both rotational and vibrational states have been proposed as qubits in a quantum computer [114, 115]. Understanding the effect of collisions on these molecular DOF will be critical to experimental implementations.

Compared to the study of atomic collisions [116], the study of cold molecular collisions is still in its infancy. Despite recent progress in molecule-molecule collision

experiments [54, 117, 118], molecule-atom collisions remain a benchmark platform for understanding of these new systems, particularly in the case of rotational and vibrational state-changing processes. Photo association [119], Stark deceleration [120, 121] and buffer-gas cooling [83] are the main experimental tools to study such collisions. Photo association enables study at ultracold temperatures, but is currently limited to molecules formed by alkali and alkaline earth atoms [119]. Stark deceleration allows tunable collisional energy with $\sim$ 1 K resolution, but so far can probe only energies above $\sim$ 30 K [83]. Buffer gas cooling provides access to temperatures of $\sim$ 0.5 K, and for a very wide range of species.

## Experimental Setup

At the heart of this work is the production of a gas of cold ThO molecules in the presence of cold $^3$He. We produce cold ThO molecules using the technique of buffer gas cooling. Using a dilution refrigerator, we cool a copper cell to a temperature of 0.8–4 K (Sect. 2.3). We ablate a $ThO_2$ ceramic target with a YAG laser pulse (a few mJ within 10 ns) to produce ThO molecules, which then collide with $^3$He and thermalize their translational motion to the cell's temperature. To calibrate the density of $^3$He, we simultaneously ablate chromium (Cr) metal to produce a gas of cold atomic Cr and measure the Cr diffusion rate in the buffer gas. Cr is detected via laser absorption spectroscopy using the $3d^5(6S)\ 4s\ (a\ ^7S_3) \rightarrow 3d^5(6S)\ 4p\ (z\ ^7P_4)$ transition at 426 nm. We use the value of $\sigma_d = 1.1\times10^{-14}$ cm$^2$ for the Cr-$^3$He diffusion cross section, which was determined in a previous experiment [86]. Becaue $\sigma_d$ can vary with temperature, as observed in other atomic [102, 103] and molecular systems [122], we include this effect as a systematic error. As we discuss in Sect. 4.2, the observed decay time of ground state ThO is affected by formation of van der Waals

complex, therefore cross calibration of $^3$He density with Cr is required for measuring the ratio between elastic and inelastic cross sections.

## 4.2 van der Waals molecule formation

ThO molecules have been predicted [123] to form ThO-He van der Waals (vdW) molecules in the presence of dense helium gas below 10 K (Fig. 4.4). Noble gas vdW molecules have been studied in a wide range of experiments, including supersonic jets [124], bulk liquid helium [125] and buffer gas cells [69], and helium vdW molecules in particular remain an active area of research. The formation of these molecules contributes to new mechanism for spin relaxation in trapped Ag atoms [69]. Li–He, the weakest bound alkaline-helium molecule, was detected only recently [70]. Here we report evidence for ThO–He molecule formation by seeing its effect on the decay time of ThO. In our setup, vdW molecules can be formed via a 3-body recombination process.

$$\mathrm{ThO} + \mathrm{He} + \mathrm{He} \underset{\Gamma_2}{\overset{\Gamma_3}{\rightleftharpoons}} \mathrm{ThO} - \mathrm{He} + \mathrm{He} \tag{4.1}$$

where $\Gamma_2$ and $\Gamma_3$ are rate coefficients for 2-body dissociation and 3-body recombination, respectively. If we begin our experiment by injecting free ThO molecules into a gas of helium, and then the vdW molecule formation dynamics of the system can be described by:

$$\frac{d[\mathrm{ThO}]}{dt} = -\frac{\Gamma_D}{[\mathrm{He}]}[\mathrm{ThO}] + \Gamma_2[\mathrm{He}][\mathrm{ThO} - \mathrm{He}] - \Gamma_3[\mathrm{He}]^2[\mathrm{ThO}], \tag{4.2}$$

$$\frac{d[\mathrm{ThO} - \mathrm{He}]}{dt} = -\frac{\Gamma_D}{[\mathrm{He}]}[\mathrm{ThO} - \mathrm{He}] - \Gamma_2[\mathrm{He}][\mathrm{ThO} - \mathrm{He}] + \Gamma_3[\mathrm{He}]^2[\mathrm{ThO}], \tag{4.3}$$

where $\Gamma_D$ is the diffusive rate constant.

The optical density (molecule number) of free ThO molecules evolves as a sum of two exponential decays (see Fig. 4.2) with time constants given by:

$$\tau_s = \left( \frac{\Gamma_D}{[\mathrm{He}]} + \Gamma_2[\mathrm{He}] + \Gamma_3[\mathrm{He}]^2 \right)^{-1}, \tag{4.4}$$

$$\tau_l = \frac{[\mathrm{He}]}{\Gamma_D} \tag{4.5}$$

Here $\tau_s$ and $\tau_l$ represent time constants for the return to thermal equilibrium and for diffusion, respectively. By repeating the experiment at various helium densities (Fig. 4.3), we can extract these time constants. The linear dependence of $\tau_l$ on helium density confirms our interpretation that it is the diffusion time constant. From this data, we determine the ratio of $\sigma_d$ for ThO-$^3$He versus Cr-$^3$He collisions to be $(1.75 \pm 0.02)$ at 2.4 K. By fitting the $\tau_s$ data to Eq. 4.4 (Fig. 4.3), we also determine the 3-body recombination rate constant to be $\Gamma_3 = (8 \pm 2) \times 10^{-33}$ cm$^6$s$^{-1}$, which is comparable to the value of $10^{-31}$ cm$^6$s$^{-1}$ calculated for the Ag-$^3$He system [69]. Although we extract a value for $\Gamma_2$ from the fit, its interpretation is not straightforward. In Eq. 4.2 and Eq. 4.3, we simplify our model with the assumption that there is only one ThO–He vdW bound state. Under this assumption, we can write $\Gamma_2 = c \cdot e^{-kT/E_b}$ for some constant $c$ and binding energy $E_b$, both of which can be determined by repeating the experiment at a different temperature.

Although there is no specific prediction for ThO-$^3$He vdW bound states, we estimate there are about 30 such states, based on observations in other atom-$^3$He and atom-$^4$He systems [69]. If we account for the ensemble of atom-He states, $\Gamma_2$ can be written as:

$$\Gamma_2 = \sum_i c_i \cdot f_i \cdot e^{-kT/E_{b,i}} \tag{4.6}$$

where $f_i$ is the fractional occupation for bound state $i$. Unlike the measured value of $\Gamma_3$, which starts from an electronic and vibrational state, the measured value of

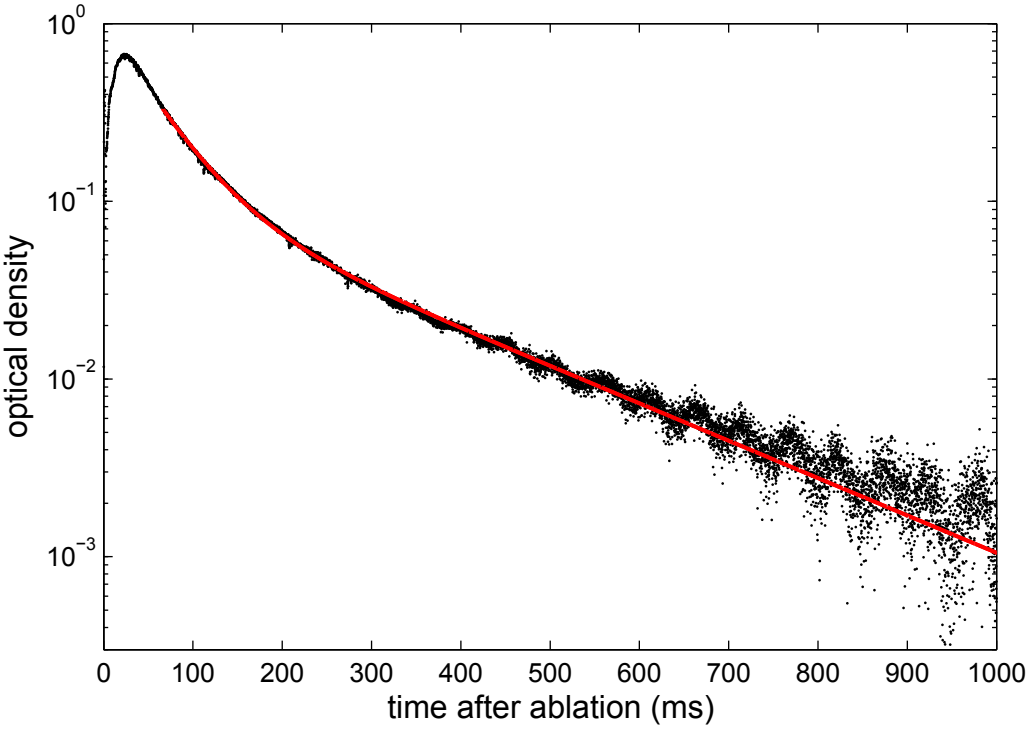


Figure 4.2: The optical density (OD) decay of ThO in its X ($\nu = 1$, J = 0) state at high helium density at 2.4 K. Solid (red) line is fit to a sum of two exponentials. We verify that both diffusion modes and temperature stabilize within the first 50 ms by observing decay of atomic chromium produced simultaneously (not shown). The apparent oscillation visible at late time (small OD) is caused by mechanical vibration of the apparatus, and it has insignificant effect on the early-time (large OD) fit.

$\Gamma_2$ is a thermal averaged rate convoluted with the formation ($f_i$) dynamics and vdW bound state-changing collisions. The highest temperature at which we observed a decay of the form predicted by Eq. 4.4 and Eq. 4.5 is 4 K, and thus we conclude there exist vdW bound states with binding energy $E_b > 4$ K.

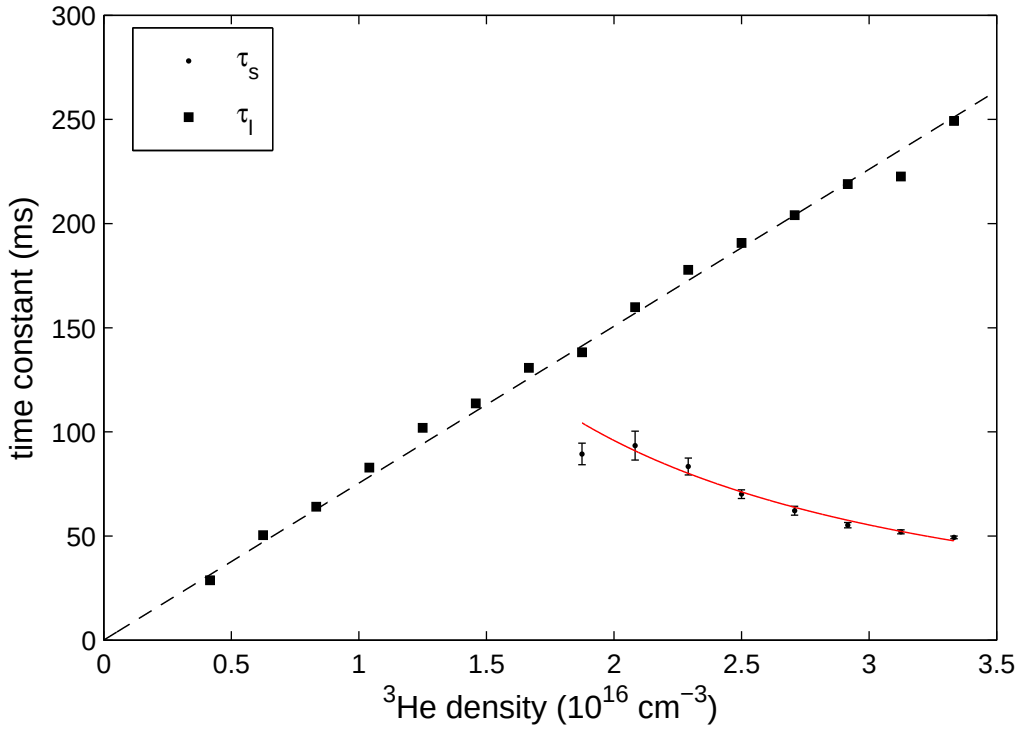


Figure 4.3: Fits to decay time constants $\tau_s$ and $\tau_l$ in Eq. 4.4 and Eq. 4.5 at various density of helium at 2.4 K. Solid squares (solid dot with error bars) denote fitted value for $\tau_l$ ($\tau_s$). Error bars are statistical. Dashed line (solid red line) is a fit to Eq. 4.5 (Eq. 4.4), where the diffusive rate constant $\Gamma_D$ (3-body recombination rate $\Gamma_3$ and 2-body decay rate $\Gamma_2$) in Eq. 4.2 is extracted.

## 4.3 Vibrational quenching in the X ($\nu = 1$, J = 0) state

There are three relevant temperature scales for the vibrational quenching of a diatomic molecule: Wigner, van der Waals (vdW), and high temperature. At intermediate temperatures, comparable to the energy of the vdW interaction, the potential can support shape and Feshbach resonances, resulting generally in an increased quenching rate at lower temperature [126]. Therefore, measurements below the vdW temperature ($\sim$ 10 K) can provide useful constraints on potential energy surfaces. Here we focus on vibrational quenching collisions between molecular thorium monoxide (ThO) and atomic $^3$He in the intermediate vdW regime.

To measure vibrational quenching in ThO molecules, we use an optical pump-and-probe technique. We transfer molecule population from the absolute ground state to the first-vibrationally-excited state via the X ($\nu = 0$) $\rightarrow$ C ($\nu = 1$) R(0) transition at 650 nm. We probe the X ($\nu = 1$) state using the X ($\nu = 0$) $\rightarrow$ C ($\nu = 1$) R(0) transition at 690 nm (Fig. 4.4). All measurements were performed in the ground rotational levels, J = 0 for the X state and J = 1 for the C state.

As shown in Fig. 4.5, laser ablation of the solid $ThO_2$ target produces significant population in the X ($\nu = 1$) state. However, such population fluctuates strongly in both magnitude and duration from shot-to-shot, presumably due to different initial populations of higher-lying states, which then decay to the $\nu = 0$ state through the $\nu = 1$ state. Hence, we cannot use the initial state population to study the dynamics of vibrational quenching.

Instead, we wait for the initial population to decay and then apply an optical pumping pulse 50 ms after ablation to transfer population from the $\nu = 0$ to the

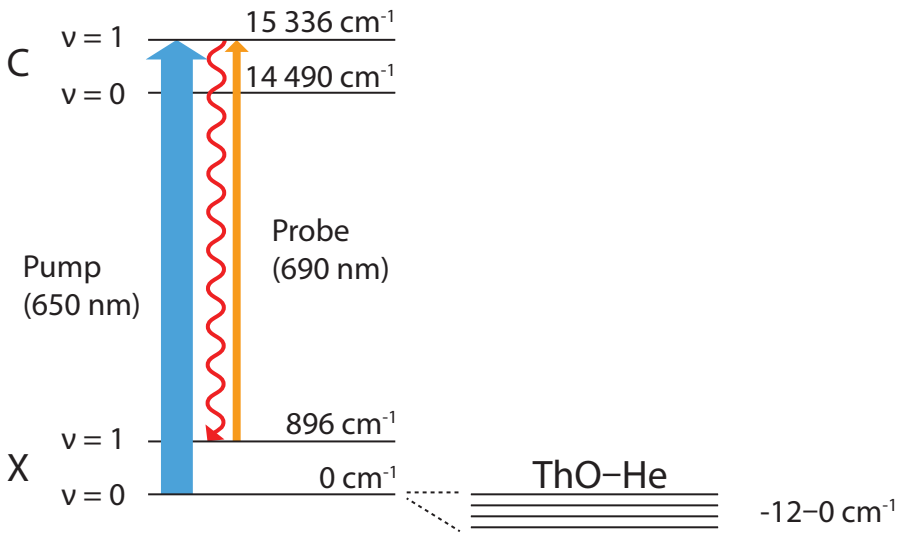


Figure 4.4: Relevant energy levels of the ThO molecule for the vibrational quenching measurement. The letters refer to the electronic states, X ($^1\Sigma^+$) and C (77% $^1\Pi$, 20% $^3\Pi$), respectively. All measurements were performed in the ground rotational levels, J = 0 for the X state and J = 1 for the C state. Optical pumping via the X ($\nu = 0$) $\rightarrow$ C ($\nu = 1$) R(0) transition at 650 nm is used to transfer population to the X ($\nu = 1$) state, which is probed using the X ($\nu = 1$) $\rightarrow$ C ($\nu = 1$) R(0) transition at 690 nm.

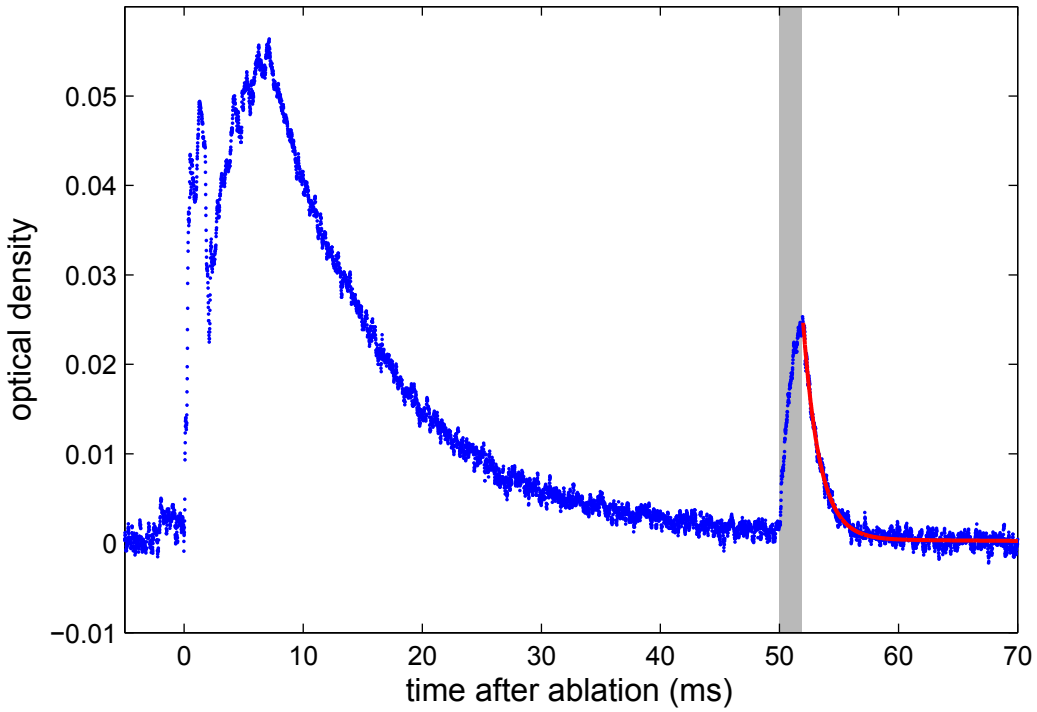


Figure 4.5: The optical density (OD) of ThO in its X ($\nu = 1$, J = 0) state at 1.2 K. The initial OD, produced by molecule production via laser ablation, exhibits strong shot-to-shot fluctuation in both magnitude and duration, and therefore, it is unsuitable for the study of vibrational quenching. At 50 ms, a short optical pumping pulse (shaded area) was used to transfer population from X ($v = 0$, J = 0) state. Solid (red) line is fit to a single exponential decay.

$\nu = 1$ state. We fit a single exponential decay to the $\nu = 1$ population created by optical pumping, and repeat the experiment at over range of helium densities. We obtain the same results when the optical pumping pulse is applied 10 ms later instead, and therefore conclude that the contribution to the fitted decay from the initial population is insignificant.

The measured ThO X ($\nu = 1$) state lifetime $\tau_\nu$ at various helium densities $n_{\mathrm{He}}$ is shown in Fig. 4.6. There are three mechanisms for decay from this state: diffusion ($\tau_d \propto n_{\mathrm{He}}$), vibrational quenching ($\tau_q \propto n_{\mathrm{He}}^{-1}$) and vdW molecule formation ($\tau_3 \propto n_{\mathrm{He}}^{-2}$).

Therefore, we may write

$$\begin{aligned} \tau_{\nu=1} &= \left(\frac{1}{\tau_d}+\frac{1}{\tau_q}+\frac{1}{\tau_3}\right)^{-1} \\ &= \left(\frac{k_d}{n_{\mathrm{He}}}+k_q n_{\mathrm{He}}+k_3 n_{\mathrm{He}}^2\right)^{-1} \end{aligned} \tag{4.7}$$

for some rate constants $k$.

When $n_{\mathrm{He}} \gtrsim 1.2\times10^{16}$ cm$^{-3}$, the effect of diffusion is insignificant. No theoretical prediction has been made for vdW molecule formation in the X ($\nu = 1$) state, so the value of $k_3$ is not known. The combined fit indicates that 3-body recombination accounts for less than 25% of the observed $\nu = 1$ decay. Under our experimental conditions, vibrational quenching is much faster ($\sim 10$ ms) than the time to thermal equilibrium between free and vdW bounded ThO molecules ($\sim 50-100$ ms), vdW complex is expected to play only a limited role in the vibrational quenching process.

We measure vibrational quenching experiment at three temperatures (Fig. 4.7). The relatively large error bar for the 800 mK measurement is caused by small signals, probably due to the lack of free ground state molecules at lower temperature to be transferred to the $\nu = 1$ state via optical pumping.

We can in principle transfer population to an initial J $> 0$ state. Because interaction potentials generally have weak functional dependence on internuclear separation compared to the angular anisotropy, mixing of rotational states in collisions is expected to be more rapid than vibrational quenching [123]. Therefore, we restrict our measurements to the J $= 0$ state.

Compared to the measured vibrational quenching rates for CaH-He [86] and the calculated value for CO-He [83], our value for ThO-$^3$He is a few orders of magnitude faster. One possible reason is that more shape and Feshbach resonances are supported by a stronger vdW interaction between ThO and $^3$He. Our results remain to be

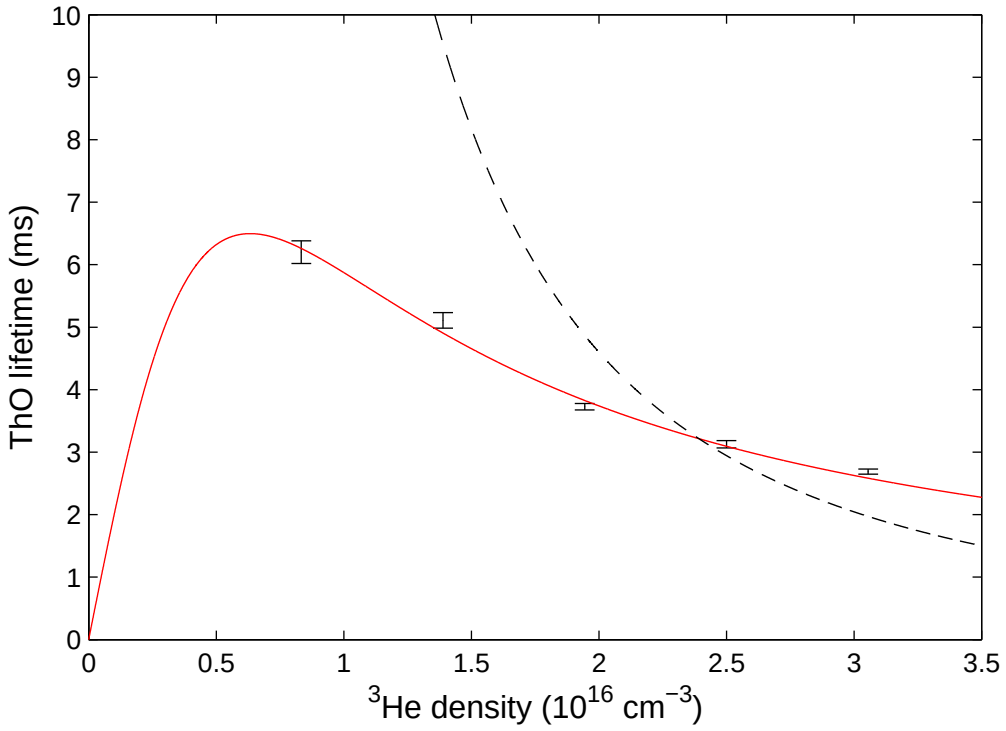


Figure 4.6: Observed vibrational quenching of the X ($\nu = 1$, J = 0) state of ThO at 1.2 K. Error bars represent statistical uncertainties. $^3$He density is determined from the diffusive decay of Cr produced simultaneously [86]. The solid red line is a combined diffusion, 2-body and 3-body fit to data (Eq. 4.7). The dashed line is a 3-body fit. The effect of diffusion is insignificant at $n_{\mathrm{He}} \gtrsim 1.2 \times 10^{16}$ cm$^{-3}$.

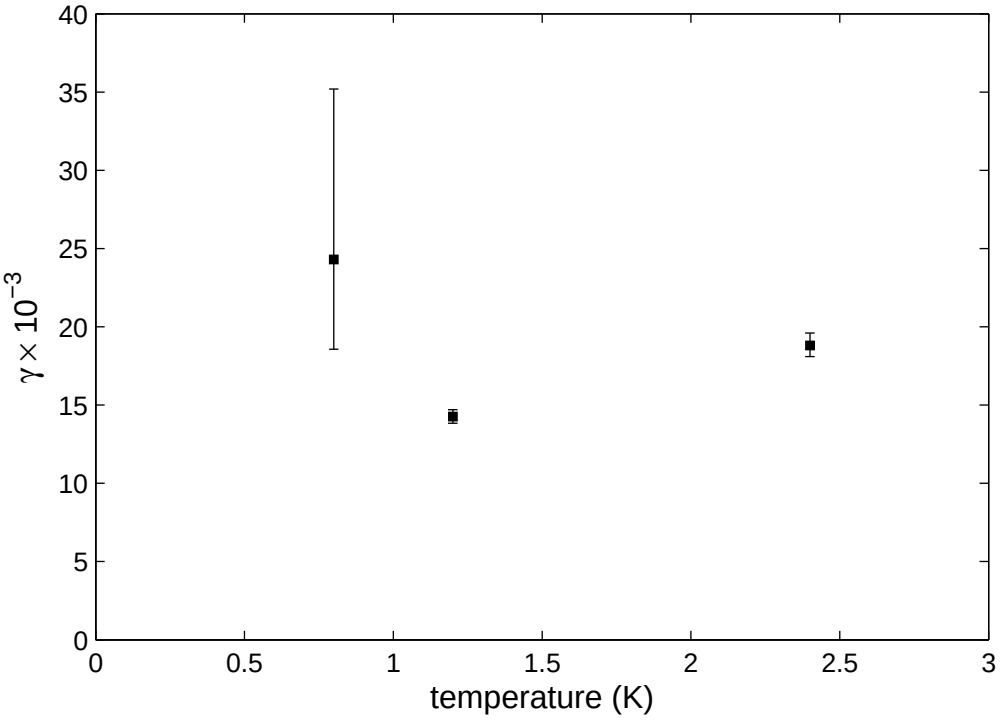


Figure 4.7: Collisional quenching of the first vibrationally excited state of ThO in collisions with $^3$He. Here we show is the ratio of the momentum-transfer to the vibrational quenching cross section for the X ($\nu = 1$, J $= 0$) state versus temperature.

explained by detailed theoretical calculations; however, we can compare our results to those obtained in other molecular systems.

## 4.4 Excited H-state and its radiative lifetime

Sect. 3.5 describes the study of the metastable first excited state in atomic thorium, and we discover the great stability of Th ($^3P_0$). In this section, using a similar optical pump-and-probe technique, we extend our study of metastable collisions to include the first electronic excited H-state in molecular ThO. We also attempt to improve previous measurements [127, 128] of the H-state radiative lifetime, but fail to do so due to unknown effects.

### 4.4.1 Previous measurements

In Ref. [127, 128], the authors reported the observation of long-lived H-state ThO produced by the initial laser ablation. To isolate this effect from the radiative decay of the H state, they transferred population from the ground X-state to the H-state using optical pumping via the A-state. They report a value for the H-state radiative lifetime $\tau_{ra} \gtrsim 1.8$ ms.

As discussed below, we employ an identical optical pumping and absorption detection scheme. We also observe the background H-state OD produced by the initial laser ablation (Fig. 4.9a). Compared to the previous measurement, our cell has a factor of 3 larger radius and a factor of 4 lower temperature, resulting in a factor of 6 longer diffusion time. This longer lifetime time allows the measurement to be performed after 20 ms, when the background H-state OD has dropped from the $10^{-2}$ to the $10^{-3}$ levels. This enables a more careful study of the H-state's lifetime.

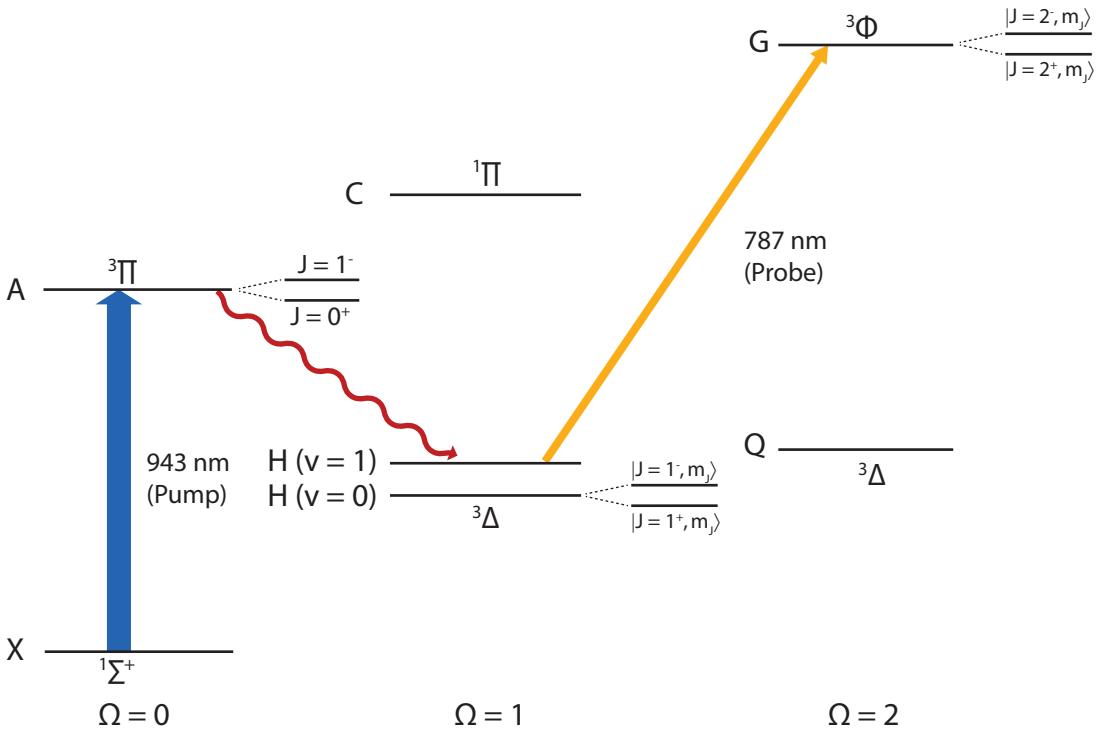


Figure 4.8: Relevant energy levels of the ThO molecule for the H-state experiment. The letters refer to the electronic states. For the X and A states, the nearest state of an opposite parity is the next rotational state (separated by ∼10 GHz). For $\Omega > 0$ states, the nearest opposite parity state is within the Ω-doublet (separated by ∼100 kHz–100 MHz). Optical pumping via the X ($\nu = 0$)→ A ($\nu = 0$) transition at 943 nm is used to transfer population to the H-state, which is probed using the H ($\nu = 0$)→ G ($\nu = 0$) transition at 787 nm. The Ω-doublets are unresolved in the experiment.

### 4.4.2 H-state preparation

When ThO molecules are produced by ablation, a long-lived H-state OD at the $10^{-3}$ level is observed for over 100 ms (Fig. 4.9a), presumably due to the decay of higher-lying states. This background H-state population fluctuates considerably in both magnitude and duration from shot-to-shot, and it shows an approximately linear dependence on helium density (Fig. 4.13).

The background population results in an optical density (OD) of $\sim 10^{-3}$, which implies that any measurements of the H-state radiative lifetime $\tau_H$ be made with a OD $> 10^{-3}$. We fulfill this requirement by filling the H-state with an OD $> 10^{-2}$ with an optical pumping pulse via the X $\rightarrow$ A transition at 943 nm (Fig. 4.8).

Consider the simplified case in which no inelastic collisions with helium occur while the molecule is in the A state ($\sim 1$ $\mu$s). Given that the Franck-Condon factor between A ($\nu = 0$) and H ($\nu = 0$) is 0.98, the optical pumping pulse should be effectively an one-way transfer from the X ($\nu = 0$) into the H ($\nu = 0$) state [128]. Furthermore, if we pump from X ($\nu = 0, \mathrm{J} = 0^+$) via A ($\nu = 0, \mathrm{J} = 1^-$), parity selection rule predicts the population will end up in the H ($\nu = 0, \mathrm{J} = 1^+, \mathrm{m_J}$) manifold (i.e. lower $\Omega$-doublet) and the H ($\nu = 0, \mathrm{J} = 2^+, \mathrm{m_J}$) manifold (i.e. lower $\Omega$-doublet), with branching ratio between $|\mathrm{J} = 1^+, \mathrm{m_J}\rangle$ and $|\mathrm{J} = 2^+, \mathrm{m_J}\rangle$ determined by the Hoenl-London factors.

In our experiment, there are two possible pathways to populate both $\Omega$-doublet components in the H ($\nu = 0, \mathrm{J} = 1$) state. First, a ThO molecule in the A state can undergo a few collisions with helium before decaying to the H state. Rotational mixing of the opposite parity A ($\nu = 0, \mathrm{J} = 0^+$) and A ($\nu = 0, \mathrm{J} = 1^-$) is expected to be rapid [123]. These opposite parity A states can then decay into either $|\mathrm{J} = 1^+, \mathrm{m_J}\rangle$ or $|\mathrm{J} = 1^-, \mathrm{m_J}\rangle$ manifolds. However, the lifetime of the A state is not known with sufficient accuracy to predict the efficiency of this process. Second, one can sup-

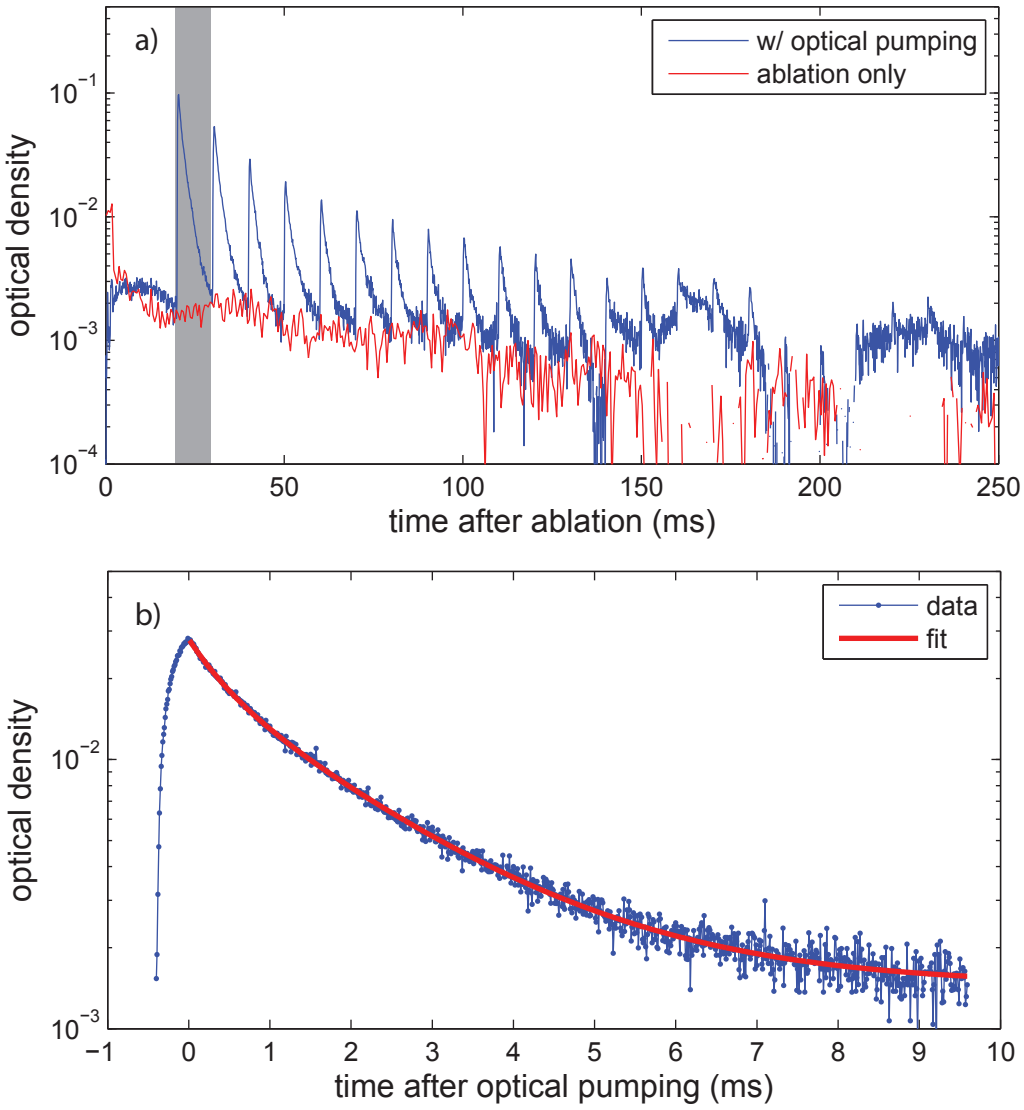


Figure 4.9: (a) The optical density (OD) of ThO H ($\nu = 0, \mathrm{J} = 1$)-state at 800 mK and $\mathrm{n_{He}} = 1.75 \times 10^{16}$ cm$^{-3}$. Measurements are performed starting 20 ms after ablation, when both diffusion modes and temperature are stabilized, as verified by a simple exponential decay of the atomic Cr OD (not shown). Even without optical pumping, there is a long-lived ThO H-state OD at the $10^{-3}$ level for over 100 ms. (b), corresponding to the shaded area in (a) after baseline substraction, shows the transfer of population to the H-state and its subsequent decay. Note that the decay is double-exponential (Eq. 4.10) as opposed the expected simple exponential for a radiative decay.

pose only the $|\mathrm{J} = 1^+, \mathrm{m_J}\rangle$ manifold is populated directly from the decay of the A ($\nu = 0, \mathrm{J} = 1^-$) state. Once populated, the $|\mathrm{J} = 1^+, \mathrm{m_J}\rangle$ is expected to be rapidly mixed with $|\mathrm{J} = 1^-, \mathrm{m_J}\rangle$ via inelastic collisions with helium [123]. The main difference between the two mechanisms is that occupation of both components of Ω-doublet in instantaneous in the first case but with a small delay in the second case.

### 4.4.3 H-state detection

The H-state is probed using absorption spectroscopy on the H ($\nu = 0$)→ G ($\nu = 0$) transition at 787 nm (Fig. 4.8). At 800 mK and zero electric field, the Ω-doublets of the both the H and G states are unresolved using the H → G transition. Ω-doublet sensitive detection can be accomplished by pumping on the H → C transition at 1090 nm and collecting the induced fluorescence (C → X) at 690 nm, since the C state has a larger Ω-doublet splitting. However, the H → C transition is about 1000 times weaker than the H → G transition, with a saturation intensity of 2 W cm$^{-2}$ instead of 1 mW cm$^{-2}$ for the H → G transition [129]. The cooling power of our dilution refrigerator therefore precludes the use of Ω-doublet resolving H → C transition.

### 4.4.4 Double-exponential decay

Either radiative decay or collisional electronic quenching of the H-state is expected to result in a simple, single exponential profile:

$$\tau_H = \left(\frac{1}{\tau_{ra}} + \frac{1}{\tau_{eq}}\right)^{-1}, \tag{4.8}$$

$$OD_H(t) = e^{-t/\tau_H} \tag{4.9}$$

where $\tau_{ra}, \tau_{eq}$'s are the lifetime for the H-state, radiative decay and electronic quenching respectively.

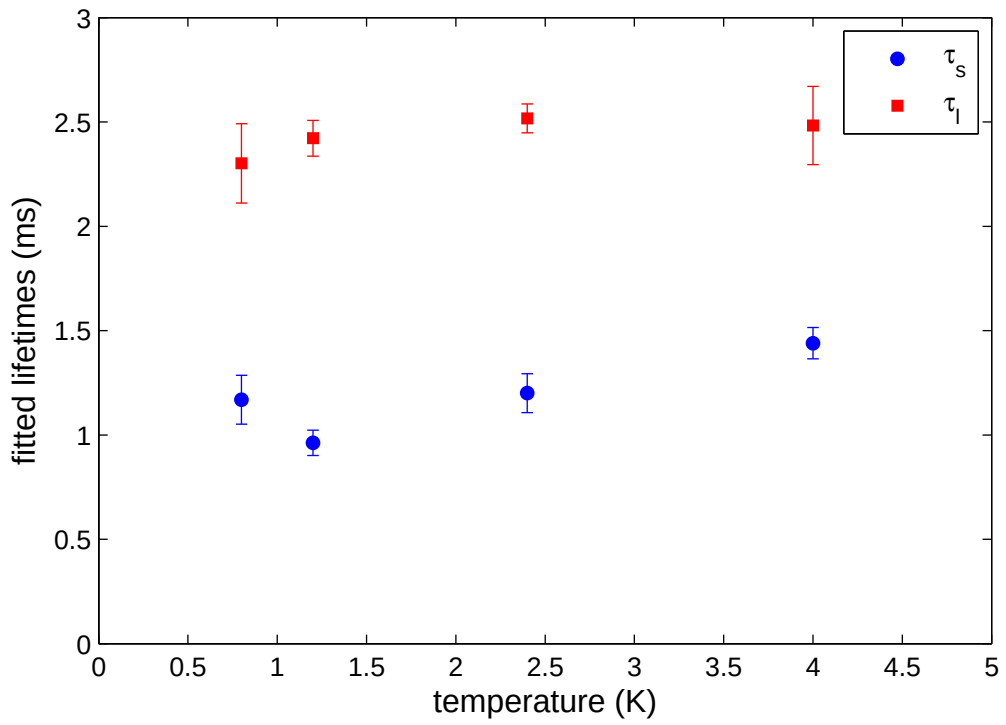


Figure 4.10: Fitted time constants (Eq.4.10) for the double-exponential decay of the ThO H-state at various temperatures.

As shown in Fig. 4.9, the optical density of the H-state after the optical pumping pulse is a double-exponential decay (Eq. 4.10) instead of the expected simple exponential decay.

$$OD_H(t) = A_s e^{-t/\tau_s} + A_l e^{-t/\tau_l} + C \tag{4.10}$$

where $s$ ($l$) denotes short (long) time component and $C$ is a constant offset, caused by background H-state OD (Eq. 4.10).

This unexpected double-exponential decay profile is robust against changes in a wide experimental parameters: laser power and duration (both pump and probe), time delay from initial ablation, helium density (Fig. 4.12), and temperature (Fig. 4.10).

In an attempt to understand the origin of the two time constants, we explore three

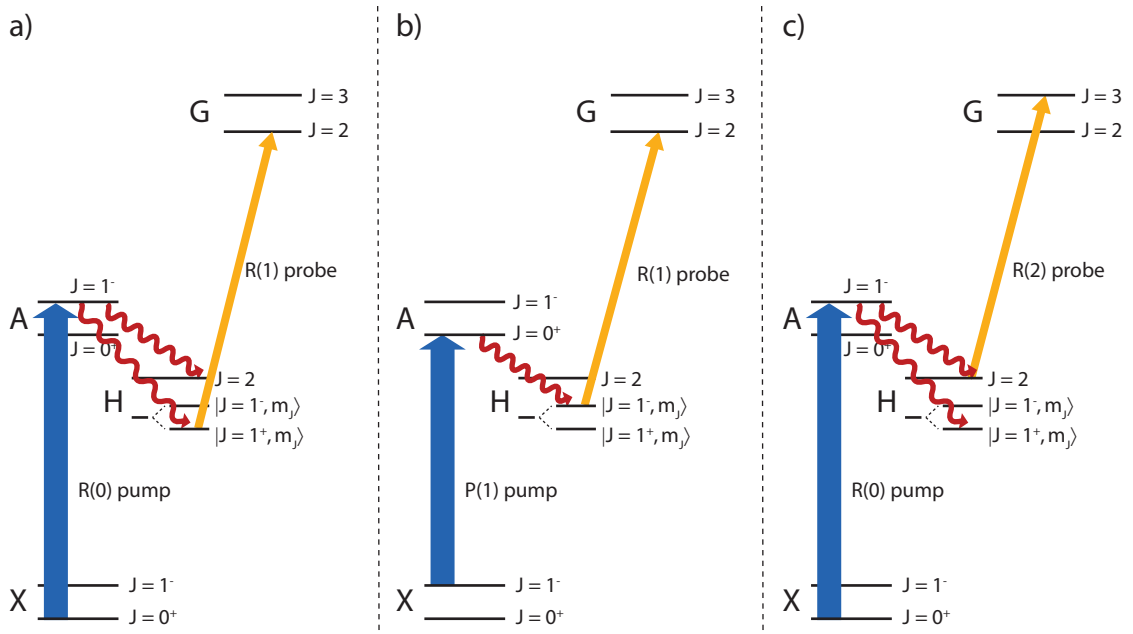


Figure 4.11: ThO H-state pump-and-probe schemes. In an effort to understand the unexpected double-exponential decay of the metastable H-state, we attempt a few pump-and-probe schemes. In the absence of inelastic collisions during the optical pumping stage, scheme (a) populates only the upper Ω-doublet of the H-state, while scheme (b) populates only the lower Ω-doublet. In scheme (c), we study the decay of the first rotationally excited (J = 2) level of the H state. The branching ratio into different rotational J states is governed by the corresponding Hoenl-London factors.

different pump-and-probe schemes (Fig. 4.11) and develop a few models. The models can be classified into two groups: a) the two components of Ω-doublet having different radiative lifetimes. b) the H-state is refilled by a metastable reservoir populated by the $X \to A \rightsquigarrow H$ optical pumping pulse.

As we discussed in Sect. 4.4.2, there is not enough information on the A state's radiative lifetime and collision mixing rates of opposite parity states to draw concrete conclusions on various pump-and-probe schemes. We discuss motivations, experimental results and their corresponding interpretations.

Consider the model in which the two time constants $\tau_s, \tau_l$ in Eq. 4.10 corresponds to the different radiative lifetimes of the two components of the Ω-doublet in the H ($\nu = 0, J = 1$) manifold. A difference in the radiative lifetimes of about 10% has been measured between the two components of the Λ-doublet in the $a^3\Pi$ state in CO [130], which is caused by perturbation from neighboring states. Ω-doubling corresponds to two projections (clockwise and anti-clockwise) of the electronic total angular momentum $J_e$ onto the internuclear axis $\hat{n}$ ($\Omega = J_e \cdot \hat{n}$), while Λ-doubling corresponds to two projections of the electronic orbital angular momentum $L_e$ onto the internuclear axis ($\Lambda = L_e \cdot \hat{n}$). The two types of doublets are therefore comparable. Although there is no expected differential perturbation of the Ω-doublet in the ThO H-state [131], we nonetheless consider such a possibility.

In cases (a) and (b) (depicted in Fig. 4.11), we attempt to create a population difference between the two components of Ω-doublet in the H ($\nu = 0, J = 1$) manifold. If the parity states were partially mixed, we would expect a different fitted values for the ratio $A_s/A_l$. In case (c), we explore a different degree of perturbation of the doublet by shifting the overall energy ($J = 2$). In this case, we would expect new values for $\tau_s$ and $\tau_l$.

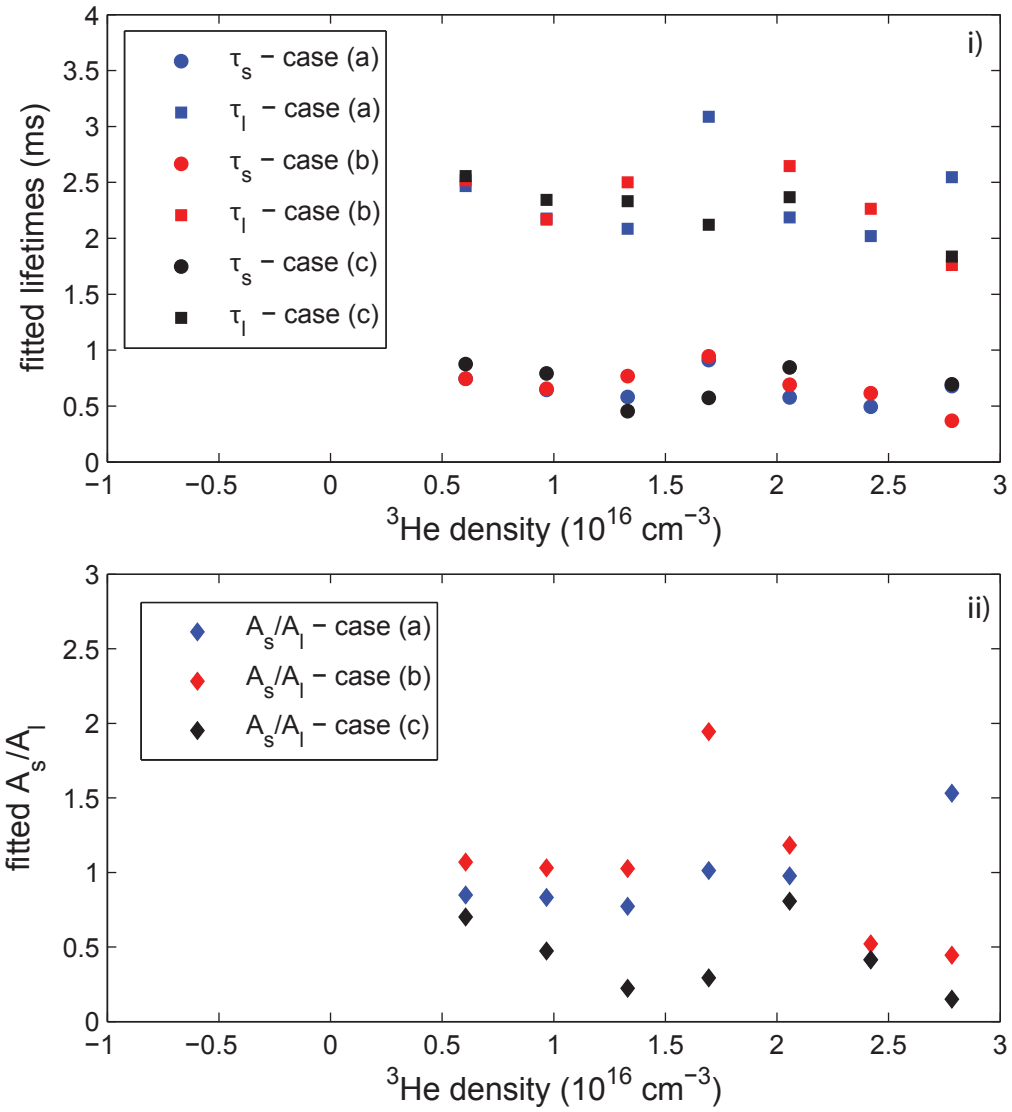


Figure 4.12: Fitted values for parameters in Eq. 4.10 under various pump-and-probe schemes (Fig. 4.11). Note that the lack of scaling of $\tau_s$ with helium density rules out van der Waals complex formation as a cause of the double-exponential decay (Sect. 4.2).

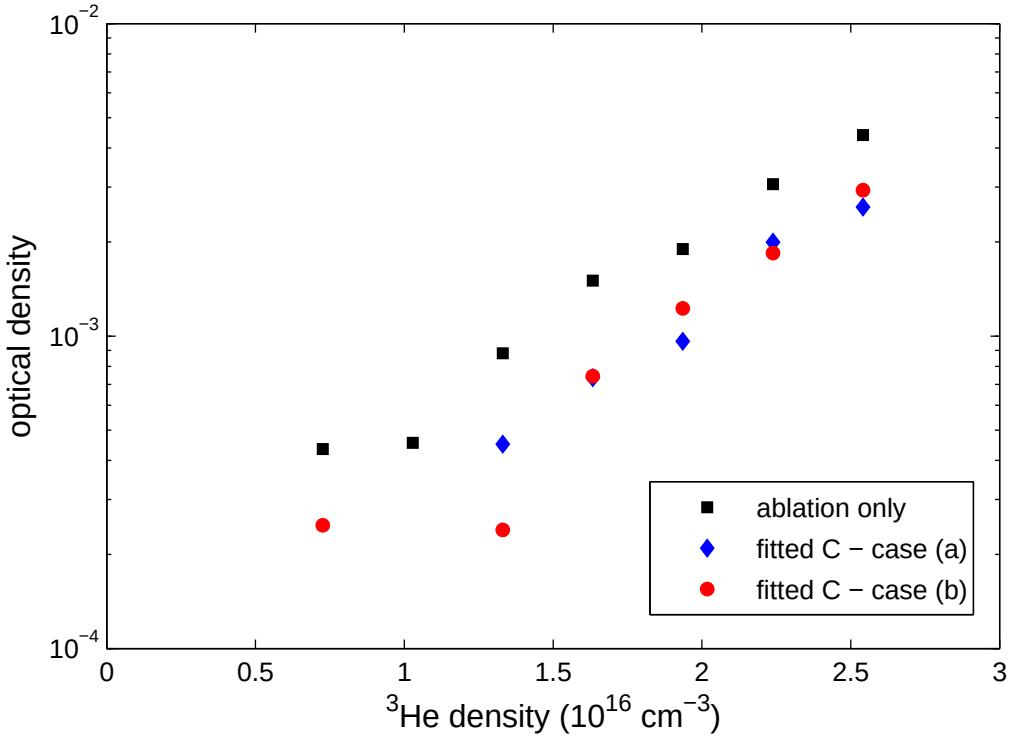


Figure 4.13: Comparison between H-state OD produced in ablation and fit parameter $C$ in Eq. 4.10. The results show that $C$ can sufficiently account OD offset populated by the initial ablation.

As shown in Fig. 4.12, various pump-and-probe schemes produce similar values for the ratio $A_s/A_l$ and time constants $\tau_s$ and $\tau_l$. We therefore conclude that the two components of the Ω-doublet probably have identical radiative lifetime. Of course, measuring the individual component radiative lifetime in a molecular beam (i.e. collisionless) using the Ω-doublet resolving H $\rightarrow$ C transition could provide a definitive conclusion.

In addition, Fig.4.13 shows that the fit parameter $C$ in Eq. 4.10 can sufficiently account for the OD offset populated by the initial ablation. Note that the lack of scaling of $\tau_s$ with helium density rules out van der Waals complex formation as a cause of the double-exponential decay (Sect. 4.2).

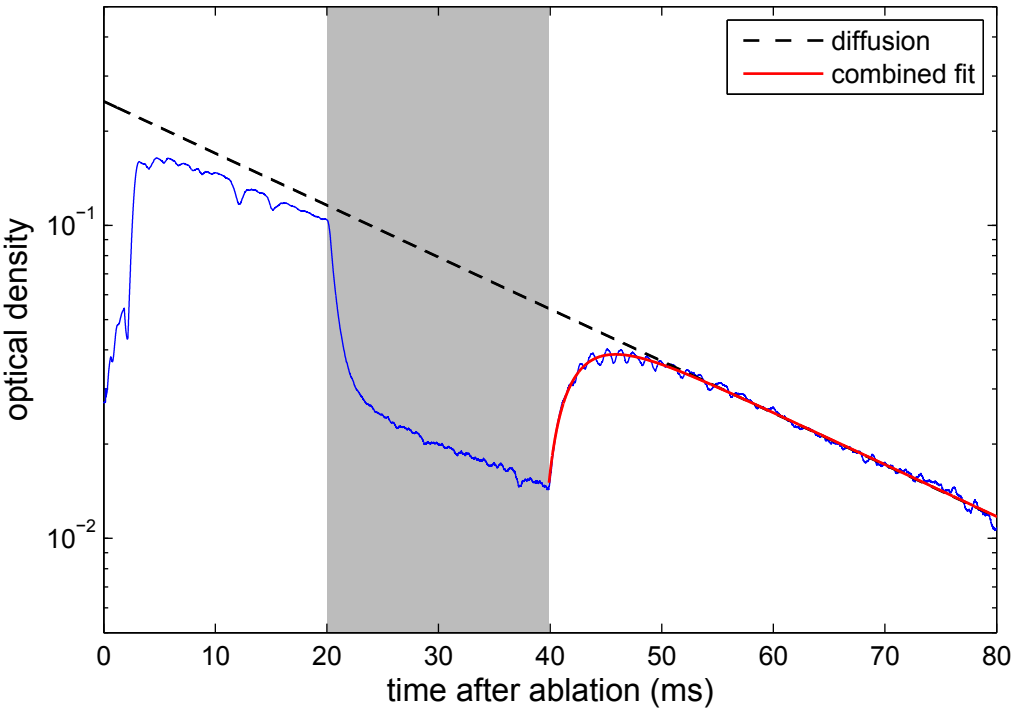


Figure 4.14: Optical depletion and recovery of the ThO X-state, which is probed using the X $\rightarrow$ C transition at 690 nm. An optical pumping pulse via the X $\rightarrow$ A transition at 943 nm is applied between 20 ms and 40 ms (shaded area). The fitted recovery time constant is $\tau_X = (3.1\pm0.1)$ ms, which is longer than $\tau_l = (2.27\pm0.07)$ ms of the H-state.

We next consider the model in which the H-state is refilled by a metastable reservoir populated by the X $\rightarrow$ A $\rightsquigarrow$ H optical pumping pulse. Reservoir states populated by initial ablation are ruled out by measurements done at various time delay after ablation.

We start our investigation of this model by measuring the recovery time of the X-state after optical depletion via the X $\rightarrow$ A transition at 943 nm (Fig. 4.14). We find the recovery time constant to be $\tau_X = (3.1 \pm 0.1)$ ms, which is longer than $\tau_l = (2.27 \pm 0.07)$ ms of the H-state. Note that this result is inconsistent with the one-way transfer promised by the 0.98 Franck-Condon factor between A ($\nu = 0$) and

H ($\nu = 0$), but the discrepancy can be explained by inelastic collisions (Sect. 4.4.2).

Suppose that there is a metastable reservoir state $\mathcal{R}$ constantly filling the lower H-state. We will explore the properties of the $\mathcal{R}$-state required to explained the observed decay profile (Fig. 4.9). We model the system using the following equations:

$$OD_H(t) = [P_R(1 - e^{-t/\tau_R}) + P_{H_0}]e^{-t/\tau_H} \tag{4.11}$$

$$OD_H(t) = [\Theta_H(t - t_D)P_R(1 - e^{-t/\tau_R}) + P_{H_0}]e^{-t/\tau_H} \tag{4.12}$$

where $P_i$'s are the initial populations immediately after the optical pumping pulse and $\tau_i$ are the radiative lifetimes. $\Theta_H$ is the Heaviside function with a reservoir activation time. It is possible the optical pumping pulse transfers population to a range of upper states which then take on average time $t_D$ to reach the metastable $\mathcal{R}$-state. Samples of resulting decay profile of the H-state is shown in Fig. 4.15. Only case (d), filling of the H-state by a reservoir with time-delayed activation, reproduces the observed double-exponential decay.

### 4.4.5 Summary and future directions

Among two models considered, filling of the H-state by a reservoir with delayed activation appears the most promising. The fact that $\tau_s$ and $\tau_l$ lacks dependence on helium density imposes a further requirement on the activation delay $t_D$ to be radiative (i.e. collisionless). A vibrationally excited H-state and the low-lying Q-state (Fig. 4.8) are two promising candidates, but the mechanism by which they might be populated by the X $\rightarrow$ A $\rightsquigarrow$ H is not understood. During our experimental run, we did not have the lasers to probe either of these states.

Given the central role played by the H-state in ThO in the ACME electron EDM search [24], the natural next step of the experiment is to measure the radiative life-

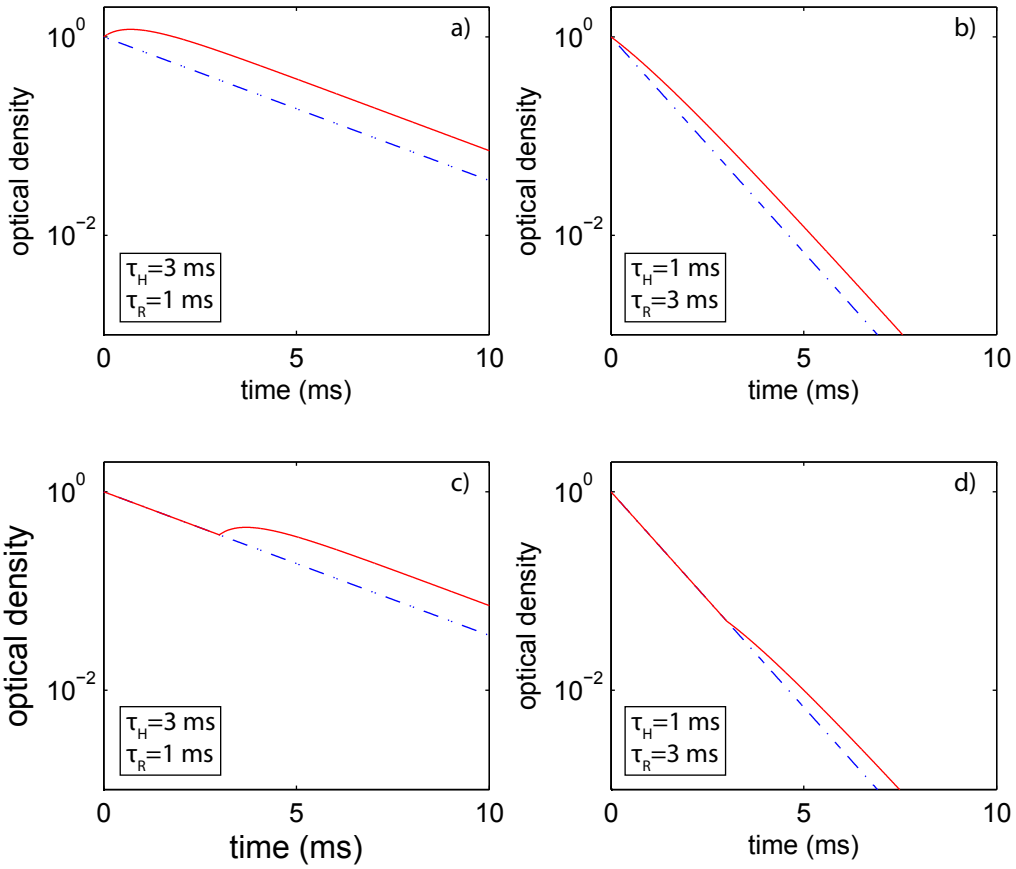


Figure 4.15: Samples of resulting decay profile of the H-state filled by a metastable reservoir $\mathcal{R}$. a) and b) correspond to Eq. 4.11; c) and d) correspond to Eq. 4.12. Without a reservoir activation delay, filling from upper states does not produce the desired decay profile (Fig. 4.9). In c) and d), $t_D = 3$ ms and the kink is an artifact caused by the abrupt turn-on of the Heaviside function. d) reproduces the observed double-exponential decay of the H-state.

time of the individual Ω-doublet component in a molecular beam (i.e. collisionless environment).

The lack of $\tau_s$ and $\tau_l$ dependence on helium density allows us to bound the radiative lifetime ($0.76 < \tau_{ra} < 2.13$) ms with 95% confidence, in agreement with the previously published value of 1.8 ms [127, 128]. We also observe no electronic quenching of the H-state even after $10^4$ collisions with $^3$He.

# Chapter 5

# Conclusion

In this thesis, we have studied the effects of anisotropic interactions in several new systems and explored a few limits of buffer gas cooling.

Unlike atomic and molecular collisions at higher temperatures, cold collisions are sensitive to the details of interaction potentials. From the external view of the colliding partner, in our case a helium atom, the internal structure (i.e. Zeeman states, rovibrational states, etc.), of an atom or a molecule is revealed through the anisotropy of the interaction potentials. Without this anisotropy, the structureless helium atom cannot influence the internal states and cannot cause an inelastic collision. Therefore, measurements of inelastic cross sections are indirect probes of the interaction anisotropy.

Due to the relatively simple, essentially structureless, electronic structure of helium, our measurements of atom-helium and molecule-helium are in an unique position to provide direct comparison between experiments and theory. Much of our data gives definitive conclusions about particle processes and await full theoretical explanation. Such theory would show in detail how internal structure manifests itself in cold collisions.

There are also several other implications of our work. "Submerged-shell physics"—the suppression of anisotropic electrostatic interactions by outer s-electrons—leads to slow Zeeman relaxation rates in transition metals [63] and in lanthanides [64]. This has led to the magnetic trapping of 7 non-S state rare-earth elements loaded by buffer gas cooling. Buffer gas cooling is very efficient in terms of atom capture fraction because it cools the entire thermal distribution. In contrast, laser cooling of atoms from an oven source only captures a small fraction of the Maxwell-Boltzmann distribution. This difference in loading efficiency could be very important for the artificially prepared elements (e.g. 85% of the actinides), for which it may be difficult to obtain samples with sufficient quantity to study. If the "submerged-shell" model carries over to the actinides, it could enable detailed study with trapped actinides atoms.

The central assumption of buffer gas cooling is that helium is inert in the cooling process. As we learned via the anomalous Zeeman relaxation of trapped silver atoms [65, 69], atoms can form van der Waals molecules (vdW) under conditions used in buffer gas cooling. This effect probably has precluded the trapping of atomic gold and is partially responsible for the rapid Zeeman relaxation observed in bismuth [101]. This effect is expected to be more important for heavier atoms. Before the work described in this thesis, it was an open question whether vdW molecule formation will affect buffer gas cooling of actinides. We now know, precisely for thorium, and more generally for actinides, that it is unlikely to be affected significantly.

A second assumption of buffer gas is that it can efficiently cool all degrees-of-freedom of an atom or a molecule. In a typical buffer gas cooling experiment, atoms and molecules are created in the gas phase at $\sim 1000$ K, along with the occupation of excited electronic, vibrational and rotational states. Although the cooling process

relies on quenching of these excited states, there are only limited experimental efforts today on the study metastable excited state collisions. In this thesis explored vibrational quenching in ThO (X, $\nu = 1$) and electronic quenching in Th ($^3P_0$) and ThO (H, $\nu = 0$).

In the first experiment on cold Th-$^3$He collisions, we use atomic thorium to study the effects of possible shielding in the actinides. This work completes the study of Zeeman relaxation across the periodic table. We find the ratio $\gamma \approx 500$ of the momentum-transfer to the Zeeman relaxation cross sections, which is well above $\gamma \sim 7$ of open-shell oxygen [100], but well below $\gamma \gtrsim 10^4$ of "submerged-shell" lanthanides. This value of $\gamma$ is too small for trapping in our apparatus. On the bright side, we did not observe any evidence for van der Waals molecule formation, providing more support for the feasibility of trapping S-state Americium in our apparatus. For future study of other actinides, our results point to the use of the recently demonstrated methods of optical loading from [43] or laser cooling of a cryogenic buffer gas beam [132], which still capture a larger fraction of the Maxwell-Boltzmann distribution than laser cooling of a traditional oven source.

We also study metastable thorium, and set a lower bound of $\gamma > 10^6$ for electronic quenching of the first excited $^3P_0$ state. This very low quenching cross section allows for the determination of a long radiative lifetime for Th ($^3P_0$) of $\tau > 134$ ms. Our results have demonstrated the feasibility of creating of cold, optically dense gases of metastable thorium similar to that of Ref. [133]. The physics of quenching of the electronic metastable states is very poorly understood. This experiment, along with other results on Yb [112] and Sr [108] present a strong challenge to theory and could lead to understanding of electronic quenching and new opportunities for applications using metastable atoms.

In the second experiment, we focus on the sparsely explored field of cold molecular collisions. We observed the predicted [123] van der Waals molecule formation and determined the 3-body recombination rate. Our results indicate that the creation of a slow cryogenic buffer gas beam of ThO using a 1 K pot [134, 135] for the next generation ACME electron EDM experiment [24] is probably not feasible. We also measured the ratio $\gamma \approx 10^4$ of the momentum-transfer to the vibrational quenching cross section for the X ($^1\Sigma^+$), $\nu = 1$, J = 0 state of ThO, which is 1000 times slower than rotational quenching. The long collisional lifetime of the $\nu = 1$ state can also lead to a wide range of applications, such as vibrational qubits [114]. Our results have added new experimental data points to the field of cold molecule collisions, and hopefully shed some lights on the questions of vibrational cooling efficiency van der Waals cluster formation. Together with the results in Ref. [56], cluster formation via both the Lindemann mechanism [74] and the 3-body recombination process have now been explored. The answers to these questions is critical for creating the high phase-space densities needed for applications such as differentiation of chiral molecules [61, 76] and mixture analysis [75].

# Appendix A

# Ruthenium-$^3$He collisions

To extend previous study of "submerged-shell" physics among the transition metals [63, 104, 136, 137], we briefly attempted to measure the Zeeman relaxation rate in atomic ruthenium-helium (Ru-$^3$He) collisions.

We use a method similar to the one used in Sect. 3.2 to produce cold ruthenium atoms. We probe the atoms using absorption spectroscopy via the $4d^7$(a $^4$F)5s ($a^5F_5$) $\rightarrow$ $4d^7$(a $^4$F)5p ($z^5F_5^\circ$) transition at 372.9 nm. The helium density is determined by the diffusion time of Ru, and we assume a Ru-$^3$He moment-transfer cross section $\sigma_d = 10^{-14}$ cm$^{-2}$.

As shown in Fig. A.2, the ratio R of population in the high-field-seeking (HFS), $m_J = J$, state to that in the low-field-seeking (LFS), $m_J = -J$, state stabilizes after $\sim$ 100 ms. This allows us to set a bound for the ratio $\gamma \lesssim 3 \times 10^4$ between the momentum-transfer to the Zeeman relaxation cross sections at 600 mK. This value of $\gamma$ is less than $\gamma = 4 \times 10^4$ for the Ti-$^3$He system [63] at 800 mK. Because of the lack optical pumping lasers, we did not employ the pump-to-probe technique to obtain a tighter bound on $\gamma$.

Table A.1: Natural abundance of isotopes of ruthenium.

| isotope | relative abundance | nuclear spin |
|---|---|---|
| 102 | 31.6% | 0 |
| 104 | 18.6% | 0 |
| 101 | 17.1% | 5/2 |
| 99 | 12.8% | 5/2 |
| 100 | 16.6% | 0 |
| 96 | 5.5% | 0 |
| 98 | 1.9% | 0 |

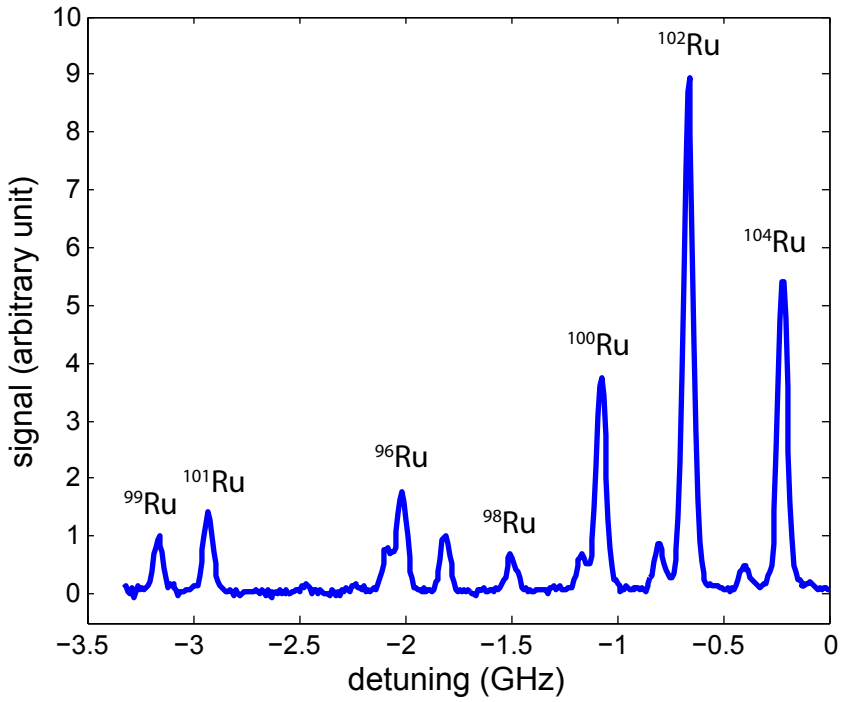


Figure A.1: Zero field spectrum of atomic ruthenium at 600 mK. The spectral peaks are identified using known isotope shifts [138].

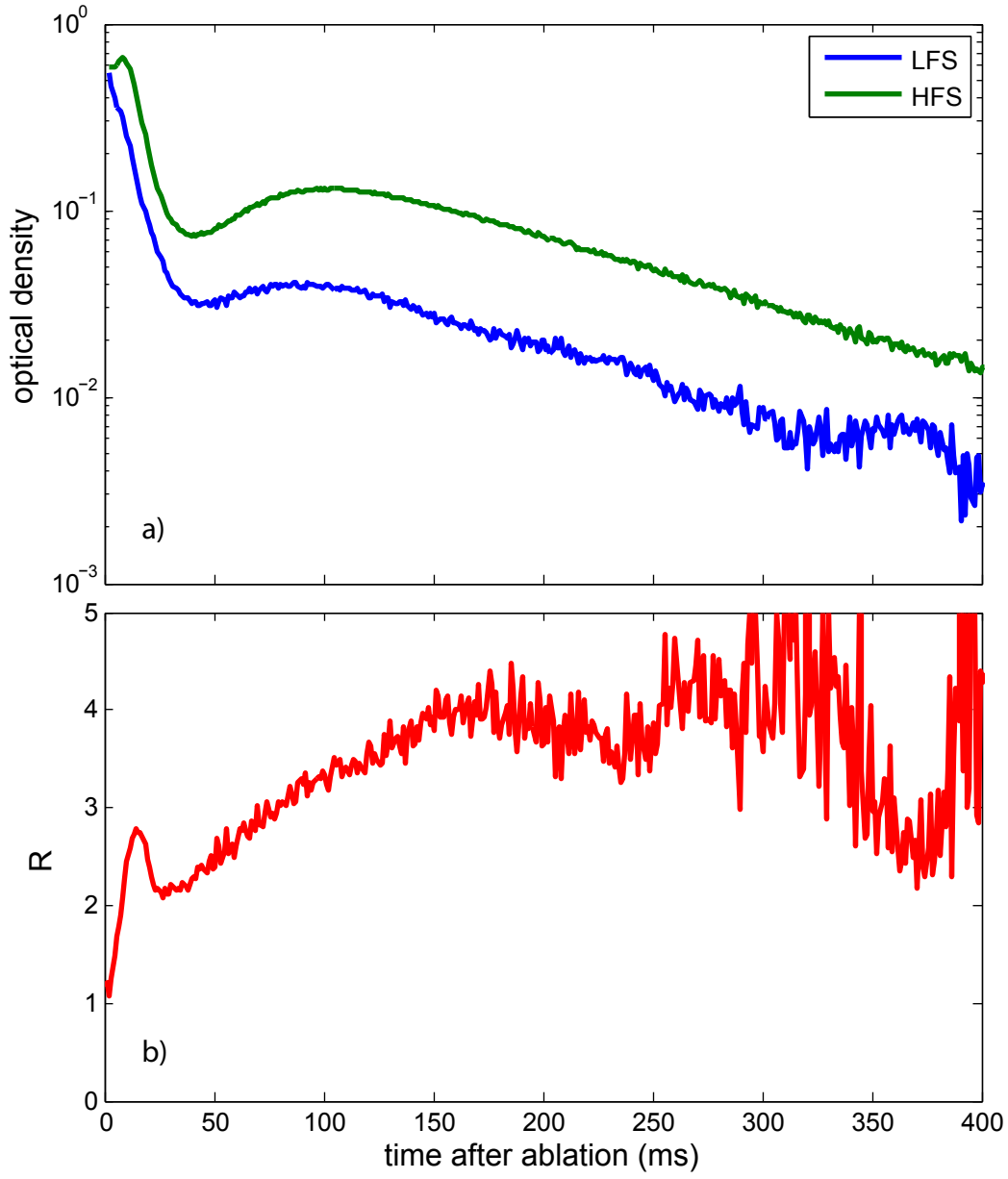


Figure A.2: a) The optical density of atomic ruthenium in the low-field-seeking (LFS), J = −J, state and the high-field-seeking (HFS), J = J, state during a Zeeman relaxation measurement. b) shows the ratio R of population in the HFS state to that in the LFS state stabilizes after ∼ 100 ms. This allows us to set a bound for the ratio $\gamma \lesssim 3 \times 10^4$ between the momentum-transfer to the Zeeman relaxation cross sections.

# Appendix B

# Optical absorption cross section

In order to extract information such as atom number, temperature and state distribution from the measured trapped spectrum, a knowledge of the optical absorption cross section is needed. The cross section can be measured or calculated. Detail derivations can be founded in Ref. [86, 139–141]. Here we provide a summary of the results that are relevant to our data analysis. We will focus on the case of a two-level atom.

## B.1 Two-state atom

Consider a laser beam traveling through a medium along the z-axis.

$$\frac{dI}{dz} = -(N_g - N_e)\sigma(\omega)I(\omega) \tag{B.1}$$

The right-hand side of Eq. B.1 is the rate of stimulated absorption in excess of stimulated emission, which in steady state equals to the rate of spontaneous emission.

$$-(N_g - N_e)\sigma I = N_e \Gamma \hbar\omega$$

Hence,

$$\sigma(\omega) = \frac{N_e}{N_e - N_g}\frac{\Gamma\hbar\omega}{I} \tag{B.2}$$

The atomic state populations are given by the steady state solution to the optical Bloch equation [141].

$$\rho_{ee} = \frac{N_e}{N} \tag{B.3}$$

$$w = \frac{N_e - N_g}{N} \tag{B.4}$$

We have,

$$\sigma(\omega) = \frac{\Omega^2/4}{(\omega-\omega_0)^2 + \Gamma^2/4}\frac{\Gamma\hbar\omega}{I} \tag{B.5}$$

$$= L(\omega)\Gamma\frac{\pi}{2}\frac{\hbar\omega}{I}\frac{\Omega^2}{\Gamma} \tag{B.6}$$

where $L(\omega)$ is the Lorentzian lineshape.

$$I = \frac{n\hbar\omega c}{V} \tag{B.7}$$

$$\frac{\hbar\omega}{I} = \frac{V}{nc} \tag{B.8}$$

The Rabi frequency is defined to be

$$\hbar\Omega = -\vec{d}\cdot\vec{E} \tag{B.9}$$

Using $\epsilon_0 E^2 = n\hbar\omega/V$,

$$\Omega^2 = \frac{n\omega_0}{\epsilon_0\hbar V}|\langle g|\vec{d}\cdot\hat{u}|e\rangle|^2 \tag{B.10}$$

where $\hat{u}$ is the spherical unit vector.

The spontaneous emission rate $\Gamma$ can be calculated using Fermi's Golden rule.

$$\Gamma = \frac{2\pi}{\hbar}|\langle i|H'|f\rangle|^2\rho_f(\hbar\omega)\delta(\hbar\omega_0) \tag{B.11}$$

where $|i\rangle = |e\rangle|n-1\rangle$, $|f\rangle = |g\rangle|n\rangle$ and[1]

$$|\langle i|H'|f\rangle|^2 = \frac{\hbar\omega}{2\epsilon_0 V}\overline{\left|\langle g|\vec{d}\cdot\vec{u}|e\rangle\right|^2} \tag{B.12}$$

Integrating over all final photon directions[2] [139],

$$\rho_f = \frac{V}{2\pi^2}\frac{\omega_0^2}{\hbar c^3} \tag{B.13}$$

$$\Gamma = \frac{\omega^3}{2\pi\epsilon_0\hbar c^3}\overline{\left|\langle g|\vec{d}\cdot\vec{u}|e\rangle\right|^2} \tag{B.14}$$

Since spontaneous emission is caused by vacuum fluctuation, we average over all possible spatial orientations of $\hat{u}$ in $\Gamma$. We obtain one-third of the dipole matrix element in $\Omega$ for that in $\Gamma$ if the optimal laser polarization is used to drive the transition.

Therefore, for optimally polarized light,

$$\sigma(\omega) \propto \frac{\Omega^2}{\Gamma} \tag{B.15}$$

$$= \frac{3\lambda_0^2}{2\pi}\frac{\Gamma^2/4}{(\omega-\omega_0)^2+\Gamma^2/4} \tag{B.16}$$

Note that on resonance, the cross section is independent of the transition strength.

$$\sigma(\omega_0) = \frac{3\lambda_0^2}{2\pi} \tag{B.17}$$

The result can be understood by noting that slower spontaneous decay in a narrow transition is compensated by a higher excitation probability on resonant.

---

[1]We have used the energy density of the zero-point radiation field, $\epsilon_0 E^2 = \hbar\omega/2V$.

[2]We do not sum over polarizations because it has already been determined by the orientations of both $\vec{d}$ and $\hat{u}$.

## B.2 Two-level atom

Next, we consider the case of a two-level atom with multiple $m_J$ states. Suppose that both atom and laser are polarized. We can calculate the contribution of the total cross section from a specific ground state $M_J$.[3]

Let's first examine the Rabi frequency.[4]

$$\Omega^2 = \frac{n\omega_0}{\epsilon_0 \hbar V} |\langle g, J, M_J | \vec{d} \cdot \hat{u} | e, J', M'_J \rangle|^2 \tag{B.18}$$

$$= \frac{n\omega}{\epsilon_0 \hbar V} |\langle g, J, M_J | d u_q | e, J', M'_J \rangle|^2 \tag{B.19}$$

Applying the Wigner-Eckart theorem,

$$\Omega^2 = \frac{n\omega}{\epsilon_0 \hbar V} \frac{|\langle g, J || d || e, J' \rangle|^2}{2J+1} |\langle J, M_J, 1, q | J', M'_J \rangle|^2 \tag{B.20}$$

The spontaneous emission rate is now an incoherent sum of decay rate through all possible channel. We can similarly apply the Wigner-Eckart theorem to each decay term.

$$\Gamma_{M'_J \to M_J} = \frac{\omega^3}{6\pi\epsilon_0 \hbar c^3} \frac{|\langle g, J || d || e, J' \rangle|^2}{2J+1} \sum_q |\langle J, M_J, 1, q | J', M'_J \rangle|^2 \tag{B.21}$$

$$\Gamma_{tot} = \sum_{M_J} \Gamma_{M'_J \to M_J} \tag{B.22}$$

$$= \frac{\omega^3}{6\pi\epsilon_0 \hbar c^3} \frac{|\langle g, J || d || e, J' \rangle|^2}{2J+1} \sum_{M_J} \sum_q |\langle J, M_J, 1, q | J', M'_J \rangle|^2 \tag{B.23}$$

$$= \frac{\omega^3}{6\pi\epsilon_0 \hbar c^3} \frac{|\langle g, J || d || e, J' \rangle|^2}{2J+1} \tag{B.24}$$

[3] In absence of other processes, we will deplete the specific group $M_J$ state through optically pumping, and a steady state will not be archieved. Therefore, at least part of the system, atom or laser field, must be unpolarized, and we will sum over different contributions to obtain the total cross section.

[4] We have chosen the polarizations such that $\vec{d}$ is along one of the basis vector $\hat{u}$.

Therefore,

$$\sigma(\omega) = \frac{3\lambda_0^2}{2\pi}\frac{\Gamma^2/4}{(\omega-\omega_0)^2+\Gamma^2/4}|\langle J, M_J, 1, q|J', M'_J\rangle|^2 \tag{B.25}$$

In the dipole approximation, light does not change the electronic spin $s$. Let's check if our result enforces such selection rule, if $L$ and $s$ are well-defined.

$$|\alpha J M_J\rangle = \sum_i C_i |\alpha L M_L\rangle |S M_S\rangle \tag{B.26}$$

where $C_i$ are the Clebsch-Gordan coefficients.

Inserting Eq. B.26 into Eq. B.20,

$$\begin{aligned}
\Omega^2 &\propto |\langle J, M_J, 1, q|J', M'_J\rangle|^2 && \text{(B.27)}\\
&= \sum_{i,j} |C_i^* C_j \langle g, L, M_L|\langle S, M_S|\langle 1, q|e, L', M'_L\rangle|S', M'_S\rangle|^2 && \text{(B.28)}\\
&= \sum_{i,j} |C_i^* C_j|^2 \cdot |\langle g, L, M_L|\langle 1, q|e, L', M'_L\rangle|^2 \cdot |\langle S M_s|S' M'_s\rangle|^2 && \text{(B.29)}\\
&\propto \sum_{\substack{S, M_S,\\ S', M'_S}} \delta_{S,S'}\delta_{M_S,M'_S} && \text{(B.30)}
\end{aligned}$$

Since $\sigma \propto \Omega^2$, our result indeed respects the $\delta S = 0$ selection rule.

## B.3 Comparison with previous results

Our results agree with appendix A in Weinstein's thesis [86], but differs from Eq. A.25 in Brahms' thesis [82]. Here we provide a table of correction factors to data previously analyzed using the Brahms' spectrum simulation code.

$$\begin{aligned}
\mathcal{F} &= \frac{\sigma_{\text{correct}}}{\sigma_{\text{Brahms 2008}}} = \frac{|\langle J, M_J, 1, q|J', M'_J\rangle|^2}{|\mathcal{A}_{l' m'_l s' m'_s l m_l s m_s q}|^2} && \text{(B.31)}\\
\mathcal{A}_{l' m'_l s' m'_s l m_l s m_s q} &= (-1)^{l'+s-m_j-q}\sqrt{(2j+1)(2j'+1)}\\
&\quad \begin{Bmatrix} s' & l' & j' \\ 1 & j & l \end{Bmatrix} \begin{pmatrix} j' & 1 & j \\ -m_j-q & q & m_j \end{pmatrix} \delta_{l',l\pm1}\delta s', s && \text{(B.32)}
\end{aligned}$$

| Element | $\mathcal{F}$ |
|---|---|
| Ag (328 nm) | 3 |
| Co (241 nm) | 9 |
| Cu (325 nm) | 3 |
| Dy (405 nm) | $195/17 \approx 11.5$ |
| Fe (248 nm) | 7 |
| Ho (411 nm) | 15 |
| Ni (232 nm) | 9 |

## B.4 Modifications to existing Matlab code

We have modified the `createDipoleHamiltonian` function in

`@AtomicTransitionJBasis/calculateHyperfine.m`

We have replaced

```
wignerTerm = (-1)^ (Le+Sg-mJe) * sqrt ((2*Jg+1)*(2*Je+1)) *...
wigner6J (Le,Je,Sg,Jg,Lg,1) * wigner3J (Jg,1,Je,mJg,sigmaLight,-mJe);
```

with

```
wignerTerm = ClebschGordan(Jg,1,Je,mJg,sigmaLight,mJe);
```

We have also commented out

```
Sg = stateG.S;
Le = stateE.L;
Se = stateE.S;
```

# Bibliography


[1] Y.S. Au, C.B. Connolly, W. Ketterle, and J.M. Doyle. Vibrational quenching of the electronic ground state in ThO in cold collisions with [sup 3]He. arXiv:1310.7264 [physics.atom-ph] (2013).

[2] Y.S. Au, C.B. Connolly, W. Ketterle, and J. M. Doyle. Properties of the ground [sup 3]F[sub 2] state and the excited [sup 3]P[sub 0] state of atomic thorium in cold collisions with [sup 3]He. arXiv:1310.7279 [physics.atom-ph] (2013).

[3] D.J. Wineland, R.E. Drullinger, and F.L. Walls. Radiation-pressure cooling of bound resonant absorbers. *Physical Review Letters* **40**, 1639 (1978).

[4] W.D. Phillips and H. Metcalf. Laser deceleration of an atomic beam. *Physical Review Letters* **48**, 596 (1982).

[5] S. A. Diddams, J. C. Bergquist, S. R. Jefferts, and C. W. Oates. Standards of time and frequency at the outset of the 21st century. *Science* **306**, 1318 (2004).

[6] M.J. Snadden, J.M. McGuirk, P. Bouyer, K.G. Haritos, and M.A. Kasevich. Measurement of the earth's gravity gradient with an atom interferometer-based gravity gradiometer. *Physical Review Letters* **81**, 971 (1998).

[7] P.W. Graham, J.M. Hogan, M.A. Kasevich, and S. Rajendran. New method for gravitational wave detection with atomic sensors. *Physical Review Letters* **110**, 171102 (2013).

[8] F. DiFilippo, V. Natarajan, K.R. Boyce, and D.E. Pritchard. Accurate atomic masses for fundamental metrology. *Physical Review Letters* **73**, 1481 (1994).

[9] H. Marion, F. Pereira Dos Santos, M. Abgrall, S. Zhang, Y. Sortais, S. Bize, I. Maksimovic, D. Calonico, J. Grnert, C. Mandache, P. Lemonde, G. Santarelli, P. Laurent, A. Clairon, and C. Salomon. Search for variations of fundamental constants using atomic fountain clocks. *Physical Review Letters* **90**, 150801 (2003).

[10] M. Fischer, N. Kolachevsky, M. Zimmermann, R. Holzwarth, Th. Udem, T. W. Hansch, M. Abgrall, J. Grunert, I. Maksimovic, S. Bize, H. Marion, F. Pereira Dos Santos, P. Lemonde, G. Santarelli, P. Laurent, A. Clairon, C. Salomon, M. Haas, U. D. Jentschura, and C. H. Keitel. New limits on the drift of fundamental constants from laboratory measurements. *Physical Review Letters* **92**, 230802 (2004).

[11] T. M. Fortier, N. Ashby, J. C. Bergquist, M. J. Delaney, S. A. Diddams, T. P. Heavner, L. Hollberg, W. M. Itano, S. R. Jefferts, K. Kim, F. Levi, L. Lorini, W. H. Oskay, T. E. Parker, J. Shirley, and J. E. Stalnaker. Precision atomic spectroscopy for improved limits on variation of the fine structure constant and local position invariance. *Physical Review Letters* **98**, 070801 (2007).

[12] H. Muller, A. Peters, and S. Chu. A precision measurement of the gravitational redshift by the interference of matter waves. *Nature* **463**, 926 (2010).

[13] A.Y. Kitaev, A.H. Shen, and M.N. Vyalyi. *Classical and quantum computation*. American Mathematical Society, 2002.

[14] M.A. Nielsen and I.L. Chuang. *Quantum computation and quantum information*. Cambridge University Press, Cambridge, U.K., 2011.

[15] W. Ketterle, D.S. Durfee, and D.M. Stamper-Kurnm. Making, probing and understanding bose-einstein condensates. In *Proceedings of the International School of Physics "Enrico Fermi", Course CXL*, 67–176 (IOS Press, Amsterdam, 1999).

[16] A.J. Leggett. Bose-einstein condensation in the alkali gases: Some fundamental concepts. *Reviews of Modern Physics* **73**, 307 (2001).

[17] W. Ketterle, D.S. Durfee, and D.M. Stamper-Kurnm. Making, probing and understanding ultracold fermi gases. In *Proceedings of the International School of Physics "Enrico Fermi", Course CLXIV* (IOS Press, Amsterdam, 2008).

[18] S. Giorgini, L.P. Pitaevskii, and S. Stringari. Theory of ultracold atomic fermi gases. *Reviews of Modern Physics* **80**, 1215 (2008).

[19] O. Morsch and M. Oberthaler. Dynamics of bose-einstein condensates in optical lattices. *Reviews of Modern Physics* **78**, 179 (2006).

[20] I. Bloch, J. Dalibard, and W. Zwerger. Many-body physics with ultracold gases. *Reviews of Modern Physics* **80**, 885 (2008).

[21] S.T. Cundiff and J. Ye. Colloquium : femtosecond optical frequency combs. *Reviews of Modern Physics* **75**, 325 (2003).

[22] L. Hollberg, C.W. Oates, E.A. Curtis, E.N. Ivanov, S.A. Diddams, T. Udem, Hugh G. Robinson, James C. Bergquist, R.J. Rafac, W.M. Itano, R.E. Drullinger, and David J. Wineland. Optical frequency standards and measurements. *IEEE Journal of Quantum Electronics* **37**, 1502 (2001).

[23] J.J. Hudson, D.M. Kara, I.J. Smallman, B.E. Sauer, M.R. Tarbutt, and E.A. Hinds. Improved measurement of the shape of the electron. *Nature* **473**, 493 (2011).

[24] ACME Collaboration, J. Baron, W.C. Campbell, D. DeMille, J.M. Doyle, G. Gabrielse, Y.V. Gurevich, P.W. Hess, N.R. Hutzler, E. Kirilov, I. Kozyryev, B.R. O'Leary, C.D. Panda, M.F. Parsons, E.S. Petrik, B. Spaun, A.C. Vutha, and A.D. West. Order of magnitude smaller limit on the electric dipole moment of the electron. *Science* **343**(6168), 269 (2014).

[25] S. Camerer, M. Korppi, A. Jockel, D. Hunger, T.W. Hansch, and P. Treutlein. Realization of an optomechanical interface between ultracold atoms and a membrane. *Physical Review Letters* **107**, 223001 (2011).

[26] J. D. Thompson, T. G. Tiecke, N. P. de Leon, J. Feist, A. V. Akimov, M. Gullans, A. S. Zibrov, V. Vuletic, and M. D. Lukin. Coupling a single trapped atom to a nanoscale optical cavity. *Science* **340**, 1202 (2013).

[27] Y.-J. Lin, R. L. Compton, K. Jimenez-Garcia, J. V. Porto, and I. B. Spielman. Synthetic magnetic fields for ultracold neutral atoms. *Nature* **462**, 462 (2009).

[28] J. Struck, M. Weinberg, C. Olschlager, P. Windpassinger, J. Simonet, K. Sengstock, R. Hoppner, P. Hauke, A. Eckardt, M. Lewenstein, and L. Mathey. Engineering ising-xy spin-models in a triangular lattice using tunable artificial gauge fields. *Nature Physics* **9**, 738 (2013).

[29] P. Richerme, C. Senko, S. Korenblit, J. Smith, A. Lee, R. Islam, W. C. Campbell, and C. Monroe. Quantum catalysis of magnetic phase transitions in a quantum simulator. *Physical Review Letters* **111**, 100506 (2013).

[30] T. Koch, T. Lahaye, J. Metz, B. Frohlich, A. Griesmaier, and T. Pfau. Stabilization of a purely dipolar quantum gas against collapse. *Nature Physics* **4**, 218 (2008).

[31] M. Lu, N.Q. Burdick, and B.L. Lev. Quantum degenerate dipolar Fermi gas. *Physical Review Letters* **108**, 215301 (2012).

[32] K. Aikawa, A. Frisch, M. Mark, S. Baier, A. Rietzler, R. Grimm, and F. Ferlaino. Bose-Einstein condensation of erbium. *Physical Review Letters* **108**, 210401 (2012).

[33] A. Andre, D. DeMille, J. M. Doyle, M. D. Lukin, S. E. Maxwell, P. Rabl, R. J. Schoelkopf, and P. Zoller. A coherent all-electrical interface between polar molecules and mesoscopic superconducting resonators. *Nature Physics* **2**, 636 (2006).

[34] Iosif .B. Khriplovich and Steve K. Lamoreaux, editors. *Cp Violation Without Strangeness*. Springer (Berlin), 1997.

[35] A. Derevianko and H. Katori. Colloquium : physics of optical lattice clocks. *Reviews of Modern Physics* **83**, 331 (2011).

[36] V.I. Yudin, A.V. Taichenachev, M.V. Okhapkin, S.N. Bagayev, Chr. Tamm, E. Peik, N. Huntemann, T.E. Mehlstaubler, and F. Riehle. Atomic clocks with suppressed blackbody radiation shift. *Physical Review Letters* **107**, 030801 (2011).

[37] K.B. Davis, M.-O. Mewes, and W. Ketterle. An analytical model for evaporative cooling of atoms. *Applied Physics B* **60**, 155 (1995).

[38] C. Chin, R. Grimm, P. Julienne, and E. Tiesinga. Feshbach resonances in ultracold gases. *Reviews of Modern Physics* **82**, 1225 (2010).

[39] K.M. Jones, E. Tiesinga, P.D. Lett, and P.S. Julienne. Ultracold photoassociation spectroscopy: Long-range molecules and atomic scattering. *Reviews of Modern Physics* **78**, 483 (2006).

[40] K.-K. Ni, S. Ospelkaus, M. H. G. de Miranda, A. Pe'er, B. Neyenhuis, J. J. Zirbel, S. Kotochigova, P. S. Julienne, D. S. Jin, and J. Ye. A high phase-space-density gas of polar molecules. *Science* **322**, 231 (2008).

[41] S. Ospelkaus, K.-K. Ni, D. Wang, M.H.G. de Miranda, B. Neyenhuis, G. Quemener, P.S. Julienne, J.L. Bohn, D.S. Jin, and J. Ye. Quantum-state controlled chemical reactions of ultracold potassium-rubidium molecules. *Science* **327**, 853 (2010).

[42] B. Yan, S.A. Moses, B. Gadway, J.P. Covey, K.R.A. Hazzard, A.M. Rey, D.S. Jin, and J. Ye. Observation of dipolar spin-exchange interactions with lattice-confined polar molecules. *Nature* **501**, 521 (2013).

[43] H.-I Lu, I. Kozyryev, B. Hemmerling, J. Piskorski, and J.M. Doyle. Magnetic trapping of molecules via optical loading and magnetic slowing. arXiv:1310.2669 [physics.atom-ph] (2013).

[44] M.D. Rosa. Laser-cooling molecules. *The European Physical Journal D* **31**, 395 (2004).

[45] J.F. Barry, E.S. Shuman, E.B. Norrgard, and D. DeMille. Laser radiation pressure slowing of a molecular beam. *Physical Review Letters* **108**, 103002 (2012).

[46] M.T. Hummon, M. Yeo, B.K. Stuhl, A.L. Collopy, Y. Xia, and J. Ye. 2d magneto-optical trapping of diatomic molecules. *Physical Review Letters* **110**, 143001 (2013).

[47] M.S. Elioff, J.J. Valentini, and D.W. Chandler. Subkelvin cooling no molecules via "billiard-like" collisions with argon. *Science* **302**, 1940 (2003).

[48] J.J. Kay, S.Y.T. van de Meerakker, K.E. Strecker, and D.W. Chandler. Production of cold nd[sub 3] by kinematic cooling. *Faraday Discussions* **142**, 143 (2009).

[49] S.Y.T. van de Meerakker, H.L. Bethlem, and G. Meijer. Laser radiation pressure slowing of a molecular beam. *Nature Physics* **4**, 595 (2008).

[50] E. Narevicius, A. Libson, C.G. Parthey, I. Chavez, J. Narevicius, U. Even, and M.G. Raizen. Stopping supersonic beams with a series of pulsed electromagnetic coils: an atomic coilgun. *Physical Review Letters* **100**, 093003 (2008).

[51] R. deCarvalho, J. M. Doyle, B. Friedrich, T. Guillet, J. Kim, D. Patterson, and J. D. Weinstein. Buffer-gas loaded magnetic traps for atoms and molecules. *The European Physical Journal D* **309**, 289 (1999).

[52] H.L. Bethlem, G. Berden, A.J.A. van Roij, F.M.H. Crompvoets, and G. Meijer. Trapping neutral molecules in a traveling potential well. *Physical Review Letters* **84**, 5744 (2000).

[53] H.L. Bethlem, G. Berden, F.M.H. Crompvoets, R.T. Jongma, A.J.A. van Roij, and G. Meijer. Electrostatic trapping of ammonia molecules. *Nature Physics* **4**, 595 (2008).

[54] B.K. Stuhl, M.T. Hummon, M. Yeo, G. Quemener, J.L. Bohn, and J. Ye. Evaporative cooling of the dipolar hydroxyl radical. *Nature* **492**, 396 (2012).

[55] W. Campbell, T. Tscherbul, H.-I. Lu, E. Tsikata, R. Krems, and J. Doyle. Mechanism of collisional spin relaxation in Σ[sub 3] molecules. *Physical Review Letters* **102**, 013003 (2009).

[56] D. Patterson, E. Tsikata, and J.M. Doyle. Cooling and collisions of large gas phase molecules. *Physical Chemistry Chemical Physics* **12**, 9736 (2010).

[57] S.C. Doret, C.B. Connolly, W. Ketterle, and J.M. Doyle. Buffer-gas cooled bose-einstein condensate. *Physical Review Letters* **103**, 103005 (2009).

[58] D.G. Fried, T.C. Killian, L. Willmann, D. Landhuis, S.C. Moss, D. Kleppner, and T.J. Greytak. Bose-einstein condensation of atomic hydrogen. *Physical Review Letters* **81**, 3811 (1998).

[59] W.C. Campbell, E. Tsikata, H.-I. Lu, L.D. van Buuren, and J.M. Doyle. Magnetic trapping and zeeman relaxation of imidogen. *Physical Review Letters* **98**, 213001 (2007).

[60] M.R. Tarbutt, B.E. Sauer, J.J. Hudson, and E.A. Hinds. Design for a fountain of ybf molecules to measure the electron's electric dipole moment. *New Journal of Physics* **15**, 053034 (2013).

[61] D. Patterson, M. Schnell, and J.M. Doyle. Enantiomer-specific detection of chiral molecules via microwave spectroscopy. *Nature* **497**, 475 (2013).

[62] Roman Krems, Bretislav Friedrich, and William C. Stwalley, editors. *Cold Molecules: Theory, Experiment, Applications*. CRC Press (Boca Raton, FL), 2009.

[63] C. Hancox, S. Doret, M. Hummon, R. Krems, and J.M. Doyle. Suppression of angular momentum transfer in cold collisions of transition metal atoms in ground states with nonzero orbital angular momentum. *Physical Review Letters* **94**, 013201 (2005).

[64] C.I. Hancox, S.C. Doret, M.T. Hummon, L. Luo, and J.M. Doyle. Magnetic trapping of rare-earth atoms at millikelvin temperatures. *Nature* **431**, 281 (2004).

[65] N. Brahms, T. V. Tscherbul, P. Zhang, J. Kłos, H. R. Sadeghpour, A. Dalgarno, J. M. Doyle, and T. G. Walker. Formation of van der waals molecules in buffer-gas-cooled magnetic traps. *Physical Review Letters* **105**, 033001 (2010).

[66] C.B. Connolly, Y.S. Au, S.C. Doret, W. Ketterle, and J.M. Doyle. Large spin relaxation rates in trapped submerged-shell atoms. *Physical Review A* **81**, 010702 (2010).

[67] B.K. Newman, N. Brahms, Y.S. Au, C. Johnson, C.B. Connolly, J.M. Doyle, D. Kleppner, and T.J. Greytak. Magnetic relaxation in dysprosium-dysprosium collisions. *Physical Review A* **83**, 012713 (2011).

[68] T. Tscherbul, P. Zhang, H. Sadeghpour, A. Dalgarno, N. Brahms, Y.S. Au, and J. Doyle. Collision-induced spin depolarization of alkali-metal atoms in cold [sup 3]He gas. *Physical Review A* **78**, 060703 (2008).

[69] N. Brahms, T.V. Tscherbul, P. Zhang, J. Klos, R.C. Forrey, Y.S. Au, H.R. Sadeghpour, A. Dalgarno, J.M. Doyle, and T.G. Walker. Formation and dynamics of van der Waals molecules in buffer-gas traps. *Physical Chemistry Chemical Physics* **13**, 19125 (2011).

[70] N. Tariq, N.A. Taisan, V. Singh, and J.D. Weinstein. Spectroscopic detection of the LiHe molecule. *Physical Review Letters* **110**, 153201 (2013).

[71] Colin Connolly. *Inelastic collisions of atomic antimony, aluminum, erbium and thulium below 1 K.* PhD thesis, Harvard University, 2012.

[72] C.B. Connolly, Y.S. Au, E. Chae, T.V. Tscherbul, A.A. Buchachenko, W. Ketterle, and J.M. Doyle. Zeeman relaxation induced by spin-orbit coupling in cold antimony-helium collisions. *Physical Review A* **88**, 012707 (2013).

[73] C.B. Connolly, Y.S. Au, E. Chae, T.V. Tscherbul, A.A. Buchachenko, H.-I. Lu, W. Ketterle, and J.M. Doyle. Spin-orbit suppression of cold inelastic collisions of aluminum and helium. *Physical Review Letters* **110**, 173202 (2013).

[74] R.T. Pack, R.B. Walker, and B.K. Kendrick. Mechanisms of atomic and molecular recombination and collision-induced dissociation. *Chemical Physics Letters* **276**, 255 (1997).

[75] David Patterson. *Buffer gas cooled beams and cold molecular collisions.* PhD thesis, Harvard University, 2010.

[76] D. Patterson and J.M. Doyle. Sensitive chiral analysis via microwave three-wave mixing. *Physical Review Letters* **111**, 023008 (2013).

[77] J.M. Doyle, J.C. Sandberg, I.A. Yu, C.L. Cesar, D. Kleppner, and T.J. Greytak. Hydrogen in the submillikelvin regime: Sticking probability on superfluid [sup 4]he. *Physical Review Letters* **67**, 603 (1991).

[78] Wesley C. Campbell and John M. Doyle. Cooling, trap loading, and beam production using a cryogenic helium buffer gas. In *Cold Molecules: Theory, Experiment, Applications,* William C Stwalley Roman Krems, Bretislav Friedrich, editor, Chapter 13, 473–508. CRC Press, Baca Raton, FL, 2010.

[79] Frank Pobell. *Matter and methods at low temperatures.* Springer, 2007.

[80] N.R. Hutzler, M.F. Parsons, Y.V. Gurevich, P.W. Hess, E. Petrik, B. Spaun, A.C. Vutha, D. DeMille, G. Gabrielse, and J.M. Doyle. A cryogenic beam of refractory, chemically reactive molecules with expansion cooling. *Physical Chemistry Chemical Physics* **13**, 18976 (2011).

[81] J.B. Hasted. *Physics of atomic collisions*. Butterworth & Co Publishers Ltd, Washington, D.C., 1972.

[82] Nathaniel Brahms. *Trapping of 1 u[sub B] atoms using buffer gas loading*. PhD thesis, Harvard University, 2008.

[83] Enrico Bodo and Franco A. Gianturco. Collisional quenching of molecular ro-vibrational energy by He buffer loading at ultralow energies. *International Reviews in Physical Chemistry* **25**, 313 (2006).

[84] Scott Nguyen. *Buffer gas loading and evaporative cooling in the multi-partial-wave regime*. PhD thesis, Harvard University, 2006.

[85] Cindy Hancox. *Magnetic Trapping of transition-metal and rare-earth atoms using buffer gas loading*. PhD thesis, Harvard University, 2005.

[86] Jonathan Weinstein. *Magnetic trapping of atomic chromium and molecular calcium monohydride*. PhD thesis, Harvard University, 2001.

[87] S.V. Nguyen, R. deCarvalho, and J.M. Doyle. Cold [sup 52]cr elastic and inelastic collision-rate determination using evaporative cooling analysis. *Physical Review A* **75**, 062706 (2007).

[88] Wesley Campbell. *Magnetic trapping of imidogen molecules*. PhD thesis, Harvard University, 2008.

[89] V. Singh, K.S. Hardman, N. Tariq, M.-J. Lu, A. Ellis, M.J. Morrison, and J.D. Weinstein. Chemical reactions of atomic lithium and molecular calcium monohydride at 1 k. *Physical Review Letters* **108**, 203201 (2012).

[90] W.H. Wing. On neutral particle trapping in quasistatic electromagnetic fields. *Progress in Quantum Electronics* **8**, 181 (1984).

[91] Rudolf Grimm, Matthias Weidemuller, and Yurii B. Ovchinnikov. Optical dipole traps for neutral atoms. In *Advances In Atomic, Molecular, and Optical Physics,* Benjamin Bederson and Herbert Walther, editors, Volume 42 of *Advances In Atomic, Molecular, and Optical Physics*, 95 – 170. Academic Press, 2000.

[92] S. Schlunk, A. Marian, P. Geng, A.P. Mosk, G. Meijer, and W. Schoelkopf, R. J.llkopf. Trapping of rb atoms by ac electric fields. *Physical Review Letters* **98**, 223002 (2007).

[93] J. van Veldhoven, H.L. Bethlem, and G. Meijer. Ac electric trap for ground-state molecules. *Physical Review Letters* **94**, 083001 (2005).

[94] S.Y.T. van de Meerakker, P.H.M. Smeets, N. Vanhaecke, R.T. Jongma, and G. Meijer. Deceleration and electrostatic trapping of oh radicals. *Physical Review Letters* **94**, 023004 (2005).

[95] J.G.E. Harris, R.A. Michniak, S.V. Nguyen, W.C. Campbell, D. Egorov, S.E. Maxwell, L.D. van Buuren, and J.M. Doyle. Deep superconducting magnetic traps for neutral atoms and molecules. *Review of Scientific Instruments* **75**(1), 17 (2004).

[96] Robert Michniak. *Enchance buffer gas loading: cooling and trapping of atoms with low effective magnetic moments*. PhD thesis, Harvard University, 2004.

[97] Edem Tsikata. *Magnetic trapping and thermal isolation of nh molecules using the buffer gas technique*. PhD thesis, Harvard University, 2009.

[98] S. Charles Doret. *A buffer-gas cooled Bose-Einstein condensate*. PhD thesis, Harvard University, 2009.

[99] J.M. Bakker, M. Stoll, D.R. Weise, O. Vogelsang, G. Meijer, and A. Peters. Magnetic trapping of buffer-gas-cooled chromium atoms and prospects for the extension to paramagnetic molecules. *Journal of Physics B: Atomic, Molecular and Optical Physics* **39**, S1111 (2006).

[100] R. Krems and A. Dalgarno. Disalignment transitions in cold collisions [sup 3]P atoms with structureless targets in a magnetic field. *Physical Review A* **68**, 013406 (2003).

[101] S. Maxwell, M. Hummon, Y. Wang, A. Buchachenko, R. Krems, and J. Doyle. Spin-orbit interaction and large inelastic rates in bismuth-helium collisions. *Physical Review A* **78**, 042706 (2008).

[102] T. V. Tscherbul, A. A. Buchachenko, A. Dalgarno, M.-J. Lu, and J. D. Weinstein. Suppression of zeeman relaxation in cold collisions of [sup 2]p[sub 1/2] atoms. *Physical Review A* **80**, 040701 (2009).

[103] M.-J. Lu, K.S. Hardman, J.D. Weinstein, and B. Zygelman. Fine-structure-changing collisions in atomic titanium. *Physical Review A* **77**, 060701 (2008).

[104] M.-J. Lu, V. Singh, and J. Weinstein. Inelastic titanium-titanium collisions. *Physical Review A* **79**, 050702 (2009).

[105] C Corliss and W.R. Bozman. *NBS monograph 53*. National Bureau of Standards, Washington, D.C., 1962.

[106] Joseph J. Katz and Glenn T. Seaborg. *The chemistry of the actinide elements*. John Wiley and Sons, Inc., New York, 1957.

[107] C. Johnson, B. Newman, N. Brahms, J.M. Doyle, D. Kleppner, and T.J. Greytak. Zeeman relaxation of cold atomic iron and nickel in collisions with [sup 3]He. *Physical Review A* **81**, 062706 (2010).

[108] A. Traverso, R. Chakraborty, Y. Martinez de Escobar, P. Mickelson, S. Nagel, M. Yan, and T. Killian. Inelastic and elastic collision rates for triplet states of ultracold strontium. *Physical Review A* **79**, 060702 (2009).

[109] J. F. Kelly, M. Harris, and A. Gallagher. Collisional transfer within the Sr (5 [sup 3]P[sup ∘][sub J]) multiplet due to nearly adiabatic collisions with noble gases. *Physical Review A* **37**, 2354 (1988).

[110] C. Redondo, M. Sanchez Rayo, P. Ecija, D. Husain, and F. Casta no. Collisional dynamics of low energy states of atomic strontium following the generation of Sr(5s5p[sup 1]P[sub 1]) in the presence of Ne, Kr and Xe. *Chemical Physics Letters* **392**, 116 (2004).

[111] H.-I. Lu, J. Rasmussen, M.J. Wright, D. Patterson, and J.M. Doyle. A cold and slow molecular beam. *Physical Chemistry Chemical Physics* **13**, 18986–90 (2011).

[112] A. Yamaguchi, S. Uetake, D. Hashimoto, J.M. Doyle, and Y. Takahashi. Inelastic collisions in optically trapped ultracold metastable ytterbium. *Physical Review Letters* **101**, 233002 (2008).

[113] M. Kajita, G. Gopakumar, M. Abe, and M. Hada. Accuracy estimations of overtone vibrational transition frequencies of optically trapped [sup 174]Yb[sup 6]Li molecules. *Physical Review A* **85**, 062519 (2012).

[114] C. Tesch and R. de Vivie-Riedle. Quantum computation with vibrationally excited molecules. *Physical Review Letters* **89**, 157901 (2002).

[115] Q. Wei, S. Kais, B. Friedrich, and D. Herschbach. Entanglement of polar symmetric top molecules as candidate qubits. *The Journal of Chemical Physics* **135**, 154102 (2011).

[116] J. Weiner and P.S. Julienne. Experiments and theory in cold and ultracold collisions. *Reviews of Modern Physics* **71**, 1 (1999).

[117] B.C. Sawyer, B.K. Stuhl, M. Yeo, T.V. Tscherbul, M.T. Hummon, Y. Xia, J. Klos, D. Patterson, J.M. Doyle, and J. Ye. Cold heteromolecular dipolar collisions. *Physical Chemistry Chemical Physics* **13**, 19059–66 (2011).

[118] M. Kirste, X. Wang, H.C. Schewe, G. Meijer, K. Liu, A. van der Avoird, L.M.C. Janssen, K.B. Gubbels, G.C. Groenenboom, and S.Y.T. van de Meerakker. Quantum-state resolved bimolecular collisions of velocity-controlled OH with NO radicals. *Science* **338**, 1060 (2012).

[119] J. Ulmanis, J. Deiglmayr, M. Repp, R. Wester, and M. Weidemuller. Ultracold molecules formed by photoassociation: heteronuclear dimers, inelastic collisions, and interactions with ultrashort laser pulses. *Chemical Reviews* **112**, 4890 (2012).

[120] L. Scharfenberg, J. Klos, P.J. Dagdigian, M.H. Alexander, G. Meijer, and S.Y.T. van de Meerakker. State-to-state inelastic scattering of Stark-decelerated OH radicals with Ar atoms. *Physical Chemistry Chemical Physics* **12**, 10660 (2010).

[121] N.J. Fitch, D.A. Esteves, M.I. Fabrikant, T.C. Briles, Y. Shyur, L.P. Parazzoli, and H.J. Lewandowski. State purity of decelerated molecular beams. *Journal of Molecular Spectroscopy* **278**, 1 (2012).

[122] M.-J. Lu and J.D. Weinstein. Cold tio(x [sup 3]$\delta$) he collisions. *New Journal of Physics* **11**, 055015 (2009).

[123] T.V. Tscherbul, E.R. Sayfutyarova, A.A. Buchachenko, and A. Dalgarno. He-ThO([sup 1]$\Sigma$[sup +]) interactions at low temperatures: elastic and inelastic collisions, transport properties, and complex formation in cold [sup 4]He gas. *Journal of Chemical Physics* **134**, 144301 (2011).

[124] Jaroslaw Koperski. *Van der Waals complexes in supersonic beams: laser spectroscopy of neutral-neutral interactions.* Wiley-VCH, Weinheim, Germany, 2003.

[125] J. Persson, Q. Hui, Z. Jakubek, M. Nakamura, and M. Takami. Formation of AgHe[sub 2] exciplex in liquid helium. *Physical Review Letters* **76**, 1501 (1996).

[126] Goulven Quemener, Naduvalath Balakrishnan, and Alexander Dalgarno. Inelastic collisions and chemical reactions of molecules at ultracold temperatures. In *Cold Molecules: Theory, Experiment, Applications,* William C Stwalley Roman Krems, Bretislav Friedrich, editor, Chapter 3, 69–124. CRC Press, Baca Raton, FL, 2010.

[127] A.C. Vutha, W.C. Campbell, Y.V. Gurevich, N.R. Hutzler, M. Parsons, D. Patterson, E. Petrik, B. Spaun, J.M. Doyle, G. Gabrielse, and D. DeMille. Search for the electric dipole moment of the electron with thorium monoxide. *Journal of Physics B: Atomic, Molecular and Optical Physics* **44**, 079803 (2011).

[128] Amar Vutha. *A search for the electric dipole moment of the electron using thorium monoxide*. PhD thesis, Yale University, 2011.

[129] Yulia Gurevich. *Preliminary measurements for an electron EDM experiment in ThO*. PhD thesis, Harvard University, 2012.

[130] T. Sykora and C. R. Vidal. Lifetimes of the co metastable a[sup 3]$\pi$ (v $\leq$ 3, $\omega$, j) levels. *Journal of Chemical Physics* **110**, 6319 (1999).

[131] Robert W. Field. Private communication.

[132] B. Hemmerling, G.K. Drayna, E. Chae, A. Ravi, and J.M. Doyle. Buffer-gas loaded magneto-optical traps for Yb, Tm, Er and Ho. arXiv:1310.3239 [physics.atom-ph] (2013).

[133] S. Magkiriadou, D. Patterson, T. Nicolas, and J.M Doyle. Cold, optically dense gases of atomic rubidium. *New Journal of Physics* **13**, 023012 (2011).

[134] N.R. Hutzler, H.-I. Lu, and J.M. Doyle. The buffer gas beam: an intense, cold, and slow source for atoms and molecules. *Chemical Reviews* **112**, 4803 (2012).

[135] Hsin-I Lu. *Magnetic trapping of molecules via optical loading and magnetic slowing*. PhD thesis, Harvard University, 2013.

[136] C.I. Hancox, M.T. Hummon, S.V. Nguyen, and J.M. Doyle. Evaporative cooling of magnetically trapped atomic molybdenum. *Physical Review A* **71**, 031402 (2005).

[137] J. G. E. Harris, S. V. Nguyen, S. C. Doret, W. Ketterle, and J. M. Doyle. Spin-exchange collisions of submerged shell atoms below 1 kelvin. *Physical Review Letters* **99**, 223201 (2007).

[138] K. Murakawa. Hyperfine structure of the spectrum of ruthenium part iii. *Journal of the Physical Society of Japan* **10**, 919 (1955).

[139] Dmitry Budker, Derek Kimball, and David DeMille. *Atomic physics: an exploration through problems and solutions*. 2 edition. Oxford University Press, USA, 2008.

[140] Claude Cohen-Tannoudji, Jacques Dupont-Roc, and Gilbert Grynberg. *Atom-Photon interactions: basic processes and applications*. Wiley-VCH, 1998.

[141] Christopher J. Foot. *Atomic Physics*. 1 edition. Oxford University Press, USA, 2005.